

A NUMERICAL STUDY OF VORTICES AND TURBULENCE IN
ULTRA-COLD BOSE GASES AND SUPERFLUID HELIUM

GEORGE WILLIAM STAGG

Thesis submitted for the degree of
Doctor of Philosophy



*School of Mathematics & Statistics
Newcastle University
Newcastle upon Tyne
United Kingdom*

June 2016

Acknowledgements

I would like to thank everybody...

Abstract

Insert your abstract here.

Contents

I	Introduction	1
1	Introduction to Bose-Einstein Condensates	2
1.1	Superfluid Helium	2
1.2	Ultra-cold Bose Gases	2
1.3	Bose-Einstein Condensation	2
1.4	Macroscopic excitations: Vortices and Solitons	2
2	Theoretical Modeling of BEC	3
2.1	Mean-field description	3
2.2	The Gross-Pitaevskii Equation	3
2.3	Quasi-Two-Dimensional Gross-Pitaevskii Equation	3
2.4	Dimensionless Gross-Pitaevskii Equations	3
2.4.1	Homogeneous GPE	3
2.4.2	Trapped GPE	4
2.5	The Dissipative Gross-Pitaevskii Equation	4
2.5.1	Phenomenological dissipation	4
2.5.2	The role of the chemical potential	5
2.6	Hydrodynamic interpretation	5
2.7	A selection of analytical solutions	5
2.7.1	Density near a wall	5
2.7.2	Soliton solutions	5
2.7.3	A note on vortex solutions	5
2.8	Initial Conditions	5
2.8.1	Thomas Fermi profile of a trapped condensate	5
2.8.2	Classical Field approximation with a homogeneous condensate	6
II	Numerical Methods	7
3	Numerical Methods	8

3.1	Numerical procedures for 2D and 3D solutions	8
3.1.1	Runge-Kutta	8
3.1.2	Imaginary time convergence	8
3.1.3	Numerical stability	8
3.2	Identifying vortices	9
3.2.1	Image filters and the Gaussian kernel	11
3.3	Quantifying vortex clustering	13
3.3.1	Recursive Cluster Algorithm (RCA)	13
3.3.2	Ripley's K function	14
3.4	Tracking vortex trajectories	14
3.5	Removing vortices with phase unwrapping	14
III	Numerical Studies	15
4	Vortex deflection	16
4.1	Comparison of deflection from a vortex and an impurity	16
4.2	Special Cases	16
5	Classical-like wakes behind elliptical obstacles in Bose-Einstein condensates	17
5.1	Introduction	18
5.2	Model	19
5.3	Results: Two-Dimensional Wakes	20
5.3.1	Vortex emission from elliptical obstacles	21
5.3.2	Formation of the Bénard–von Kármán vortex street	22
5.3.3	Critical Velocity past an Elliptical Obstacle	23
5.3.4	Role of Obstacle Size and Ellipticity on the Wake	24
5.3.5	Vortex Clustering	25
5.4	Results: Three-Dimensional Wakes	26
5.4.1	Symmetric Wakes	26
5.4.2	Asymmetric Wakes	27
5.5	Conclusion	28
5.6	Model of 2D and 3D BEC with Gaussian Potentials	28
6	Decay of 2D quantum turbulence in a highly oblate Bose-Einstein condensate	30
6.1	Introduction	30
6.2	Set-Up	31
6.3	Results	32
6.3.1	Number of Vortices Generated	32
6.3.2	Stages of the Condensate Evolution	33

6.3.3	Crescent-Shaped Density Structures	37
6.3.4	Vortex Generation via an Elliptical Obstacle	38
6.4	Conclusion	38
7	Critical velocity at finite temperature	40
7.1	Strongly Non-equilibrium initial condition	40
7.2	Vortex shedding	40
7.3	Critical velocity for vortex production	40
8	Simulating the surface of a “Floppy Wire”	41
8.1	Superfluid wire experiments	41
8.2	The “Floppy Wire” AFM image	41
8.3	GPE with AFM surface	41
8.4	2D clusters and backflow vortex generation	41
8.5	3D boundary layer and velocity statistics	41
A	Detailed Derivations	42
A.1	Derivation of the Hydrodynamic Equations via the Madelung Transformation	42
A.2	Derivation of the Gross-Pitaevskii Equation through Quantum Field Theory	44
A.3	Energy	48
A.4	Force	48
Bibliography		49

Part I

Introduction

Chapter 1

Introduction to Bose-Einstein Condensates

1.1 Superfluid Helium

1.2 Ultra-cold Bose Gases

1.3 Bose-Einstein Condensation

1.4 Macroscopic excitations: Vortices and Solitons

Chapter 2

Theoretical Modeling of BEC

2.1 Mean-field description

2.2 The Gross-Pitaevskii Equation

$$i\hbar \frac{\partial \Psi(\mathbf{r}, t)}{\partial t} = \left(-\frac{\hbar^2}{2m} \nabla^2 + V(\mathbf{r}, t) + g|\Psi(\mathbf{r}, t)|^2 - \mu \right) \Psi(\mathbf{r}, t). \quad (2.1)$$

Where $V(\mathbf{r}, t) = V_{\text{obj}}(\mathbf{r}, t) + V_{\text{trap}}(\mathbf{r}, t)$. When trapped, the trap is harmonic and of the form $V_{\text{trap}} = m\omega^2 r^2/2$, otherwise $V_{\text{trap}} = 0$.

2.3 Quasi-Two-Dimensional Gross-Pitaevskii Equation

When $\omega_z \gg \omega_r$ and $\hbar\omega_z \gg \mu$ the condensate becomes highly oblate. Tight z confinement causes the dynamics to become essentially two dimensional. In this case a 2DGPE can be used to model the system where $g_{2D} = g/\left(\sqrt{2\pi}l_z\right)$. [CITE PARKER THESIS] The chemical potential is also modified. See Section 2.5.2 for details on μ .

2.4 Dimensionless Gross-Pitaevskii Equations

2.4.1 Homogeneous GPE

When discussing a homogeneous condensate we drop the dimensionless modifiers for each quantity and use the equation,

$$i\frac{\partial \psi(\mathbf{r}, t)}{\partial t} = \left(-\frac{1}{2} \nabla^2 + |\psi(\mathbf{r}, t)|^2 + V_{\text{obj}}(\mathbf{r}, t) - 1 \right) \psi(\mathbf{r}, t). \quad (2.2)$$

2.4.2 Trapped GPE

When discussing the a trapped condensate we drop the dimensionless modifiers for each quantity and use the equation,

$$i \frac{\partial \phi(\mathbf{r}, t)}{\partial t} = \left(-\frac{1}{2} \nabla^2 + g|\phi(\mathbf{r}, t)|^2 + V(\mathbf{r}, t) - 1 \right) \phi(\mathbf{r}, t). \quad (2.3)$$

Where $V(\mathbf{r}, t) = \frac{r^2}{2} + V_{\text{obj}}(\mathbf{r}, t)$

2.5 The Dissipative Gross-Pitaevskii Equation

2.5.1 Phenomenological dissipation

The GPE can be modified to provide a simple phenomenological model of a condensate's interaction with the thermal cloud. The phenomenological damping term, γ , is added to the right hand side of the GPE with the effect that the energy in the system no longer remains constant. The energy will instead vary over time to approach some constant value. This has the effect of damping out any excitations made to the condensate, and over time the wavefunction approaches the steady state. A microscopic justification for this model was provided by Penckwitt et al [CITE] and Gardiner et al [CITE]; by studying the growth of a condensate in the presence of a rotating thermal cloud an expression for γ was found.

$$\gamma = \frac{4m\tilde{g}a^2kT}{\pi\hbar^2} \approx 0.01, \quad (2.4)$$

where k is Boltzmann's constant and $\tilde{g} = 3$ is a factor used for correction. As γ is proportional to temperature, in this thesis various values of γ will be used as a qualitative probe of finite-temperature dynamics with only marginally more complex numerical methods. In the case with a homogeneous condensate this leaves us with

$$(i - \gamma) \frac{\partial \psi(\mathbf{r}, t)}{\partial t} = \left(-\frac{1}{2} \nabla^2 + |\psi(\mathbf{r}, t)|^2 + V_{\text{obj}}(\mathbf{r}, t) - 1 \right) \psi(\mathbf{r}, t), \quad (2.5)$$

and in the case with a trapped condensate this leaves us with

$$(i - \gamma) \frac{\partial \phi(\mathbf{r}, t)}{\partial t} = \left(-\frac{1}{2} \nabla^2 + g|\phi(\mathbf{r}, t)|^2 + V(\mathbf{r}, t) - 1 \right) \phi(\mathbf{r}, t). \quad (2.6)$$

2.5.2 The role of the chemical potential

2.6 Hydrodynamic interpretation

Often it can be helpful to write the GPE, via the so called Madelung transformation, as a set of hydrodynamic equations. The transformation reinterprets the wavefunction Ψ as a magnitude directly related to the fluid density and a phase which is directly related to the fluid velocity. We write the wavefunction in the form

$$\Psi(\mathbf{r}, t) = R(\mathbf{r}, t) \exp(i\theta(\mathbf{r}, t)), \quad (2.7)$$

and identify the fluid density as $\rho = mR^2$ and the velocity as $\mathbf{v} = \frac{\hbar}{m}\nabla\theta$. In vector form we obtain a continuity equation

$$\frac{\partial\rho}{\partial t} + \nabla(\rho\mathbf{v}) = 0, \quad (2.8)$$

and an equation similar to the Euler equation for an inviscid fluid,

$$\rho \left(\frac{\partial\mathbf{v}}{\partial t} + (\mathbf{v} \cdot \nabla) \mathbf{v} \right) = -\nabla p - \nabla\mathbf{P} - \rho\nabla \left(\frac{V}{m} \right). \quad (2.9)$$

where $P_{jk} = -\frac{\hbar^2}{4m^2}\rho\frac{\partial^2 \ln \rho}{\partial x_j \partial x_k}$. A detailed derivation of this result can be found in Appendix A.1.

2.7 A selection of analytical solutions

2.7.1 Density near a wall

2.7.2 Soliton solutions

$$\Psi(x) = \Psi_0 \tanh \left(\frac{x}{\sqrt{2}\xi} \right) \quad (2.10)$$

2.7.3 A note on vortex solutions

2.8 Initial Conditions

2.8.1 Thomas Fermi profile of a trapped condensate

Fixed in time Ψ and V .

$$\sqrt{\frac{\mu - V(\mathbf{r})}{g}} = \Psi(\mathbf{r}) \quad (2.11)$$

2.8.2 Classical Field approximation with a homogeneous condensate

$$\psi(\mathbf{r}, t) = \sum_{\mathbf{k}} a_{\mathbf{k}} \exp(i\mathbf{k} \cdot \mathbf{r}), \quad (2.12)$$

where the complex Fourier amplitudes $a_{\mathbf{k}}$ are related to the occupation numbers $n_{\mathbf{k}}$ through $\langle a_{\mathbf{k}} a_{\mathbf{k}'}^* \rangle = n_{\mathbf{k}} \delta_{\mathbf{k}\mathbf{k}'}$. The phase of the complex amplitudes $a_{\mathbf{k}}$ are distributed uniformly on $[0, 2\pi]$ while $|a_{\mathbf{k}}|$ is distributed randomly with fixed mean equal to unity; it has been found that different distributions of $|a_{\mathbf{k}}|$ make no qualitative difference to the turbulent evolution[phys rev A 66 013603]. [TODO: write about choice of E and N here to get different condensate fractions]

We also have the integral distribution function,

$$D_k = \sum_{k' < k} n_{\mathbf{k}}. \quad (2.13)$$

This is a coarse-grained characteristic of the particle distribution which shows how many particles have momenta less than k .

Part II

Numerical Methods

Chapter 3

Numerical Methods

3.1 Numerical procedures for 2D and 3D solutions

3.1.1 Runge-Kutta

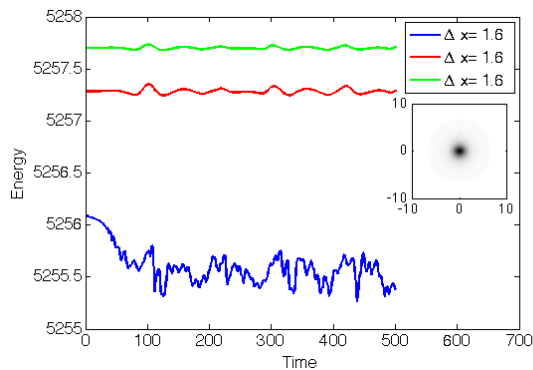
3.1.2 Imaginary time convergence

3.1.3 Numerical stability

We now systematically study the numerical stability of common simulated systems. Our aim is to find a suitable discretisation of space and time so that while simulations are timely, our numerical solutions are converged and not overly sensitive to small changes computational parameters.

We use energy to measure because in the undamped gpe energy is conserved.

We run 100 units of imaginary time stepping to get density profile We run another 100 units for vortex IC We run 500 units in real time to study stability



3.2 Identifying vortices

```

input : A  $n_x \times n_y$  field  $\theta$ . A  $n_x \times n_y$  field  $P$ . A line integral width  $l$ .
output: A  $n_x \times n_y$  field  $Q$ .

for  $i \leftarrow 1 + l/2$  to  $n_x - l/2$  do
    for  $j \leftarrow 1 + l/2$  to  $n_y - l/2$  do
        |  $Q[i, j] \leftarrow \oint_{\square} \nabla \theta \cdot ds$ , where  $\square$  is a square loop of width  $l$  centered on  $(i, j)$ ;
        | end
        | if  $P[i, j] > 1$  then  $Q[i, j] \leftarrow 0$ ;
    end

```

Algorithm 1: Initial vortex detection. Outputs a field with positive values near a vortex with circulation 1, negative values near a vortex with circulation -1 and zero valued otherwise.

```

input :A  $n_x \times n_y$  binary field  $P$ .
output:A  $n_x \times n_y$  field  $Q$ .

Let  $\text{linked}$  be a  $(n_x, n_y) \times 4$  field;
 $\text{linked} \leftarrow -1$  at every point,  $Q \leftarrow -1$  at every point;
 $\text{lc} \leftarrow 1$ ,  $\text{rc} \leftarrow 0$ ;
for  $i \leftarrow 2$  to  $n_x - 1$  do
    for  $j \leftarrow 2$  to  $n_y - 1$  do
        if  $P[i, j] = 0$  then skip this loop iteration;
        foreach  $c \in (Q[i + 1, j - 1], Q[i, j - 1], Q[i - 1, j - 1], Q[i - 1, j])$  do
            if  $c \geq 0$  then
                 $Q[i, j] \leftarrow c$ ;
                 $\text{linked}[\text{lc}, 1] \leftarrow c$ ;
            end
        end
        if  $Q[i, j] \geq 0$  then  $\text{lc} \leftarrow \text{lc} + 1$ ;
        else
             $Q[i, j] \leftarrow \text{rc}$ ;
             $\text{rc} \leftarrow \text{rc} + 1$ ;
        end
    end
end

for  $i \leftarrow 1$  to  $(n_x \times n_y)$  do
    if  $\max(\text{All elements of linked from row } i) = -1$  then continue;
     $m \leftarrow \min(\text{All elements of linked from row } i \text{ with value} \geq 0)$ ;
    for  $j \leftarrow 1$  to 4 do
        if  $\text{linked}[i, j] \neq m$  and  $\text{linked}[i, j] \geq 0$  then
            for  $k \leftarrow 1$  to  $n_x$  do
                for  $l \leftarrow 1$  to  $n_y$  do
                    if  $Q[k, l] = \text{linked}[i, j]$  then  $Q[k, l] = m$ ;
                end
            end
        end
    end
end

```

Algorithm 2: The B/W Label algorithm. Outputs a field with the same non-zero regions of the input binary field, but with each connected region labeled with a unique value.

3.2.1 Image filters and the Gaussian kernel

```

input : A  $n_x \times n_y$  field  $P$ , a Gaussian filter width  $g$ .
output: A  $n_x \times n_y$  field  $Q$ .

 $Q \leftarrow 0$  at every point;
for  $k \leftarrow 1$  to  $n_x$  do
    for  $l \leftarrow 1$  to  $n_y$  do
        for  $i \leftarrow 1$  to  $n_x$  do
            for  $j \leftarrow 1$  to  $n_y$  do
                 $| Q[k, l] \leftarrow Q[k, l] + P[i, j] \times \exp(-[(k - i)^2 + (l - j)^2]/g^2);$ 
            end
        end
         $| Q[k, l] \leftarrow Q[k, l]/(n_x \times n_y);$ 
    end
end

```

Algorithm 3: Gaussian convolution. Filters out features with structures of size less than the input filter width. The output is analogous to a ‘blurring’ of the input field. This allows high frequency noise to be removed.

```

input :A  $n_x \times n_y$  field  $\theta$ . A  $n_x \times n_y$  field  $P$ . A threshold value  $t$ .
output:Number of vortices found,  $n_v$ . Vortex location, a  $2 \times n_v$  field  $V_l$ . Vortex
polarity, a vector  $V_p$  of length  $n_v$ .

 $Q \leftarrow$  Algorithm 3  $\leftarrow$  Algorithm 1  $\leftarrow (\theta, P)$  ;
 $R \leftarrow 0$  at every point,  $S \leftarrow 0$  at every point;
 $n_v \leftarrow 0$ ;
for  $i \leftarrow 1$  to  $n_x$  do
    for  $j \leftarrow 1$  to  $n_y$  do
        if  $Q[i, j] > t$  then  $R[i, j] = 1$ ;
        if  $Q[i, j] < t$  then  $S[i, j] = 1$ ;
    end
end
foreach  $C \in (R, S)$  do
     $D \leftarrow$  Algorithm 2  $\leftarrow C$ ;
    for  $i \leftarrow 1$  to  $\max(D)$  do
         $V[1, n_v] \leftarrow$  mean row of the points where  $D = i$ ;
         $V[2, n_v] \leftarrow$  mean column of the points where  $D = i$ ;
        if  $C = R$  then  $V[3, n_v] \leftarrow 1$ ;
        if  $C = S$  then  $V[3, n_v] \leftarrow -1$ ;
         $n_v \leftarrow n_v + 1$ ;
    end
end

```

Algorithm 4: Calculate vortex locations and polarity.

3.3 Quantifying vortex clustering

3.3.1 Recursive Cluster Algorithm (RCA)

```

input : Vortex location, a  $2 \times n_v$  field  $V_l$ . Vortex polarity, a vector  $V_p$  of length  $n_v$ .
        Number of vortices,  $n_v$ .
output: Vortex decomposition, a vector  $V_{rca}$  of length  $n_v$ .

 $n_{rca} \leftarrow 0;$ 
 $V_{rca} \leftarrow 0$  at every point;
while dipoles continue to be identified do
    for  $i \leftarrow 1$  to  $n_v$  do
        if vortex  $i$  is mutual nearest neighbours with some other vortex  $j$  then
            if  $V_p[i] \neq V_p[j]$  then
                 $V_{rca}[i] \leftarrow -1;$ 
                 $V_{rca}[j] \leftarrow -1;$ 
            end
        end
    end
end

while vortices continue to be added to clusters do
    for  $i \leftarrow 1$  to  $n_v$  do
        for  $j \leftarrow 1$  to  $n_v$  do
            if  $V_{rca}[i] < 0$  or  $V_{rca}[j] < 0$  then continue;
            if vortex  $i$  and  $j$  are closer to one another than one of opposite polarity then
                if  $V_{rca}[i] > 0$  and  $V_{rca}[j] = 0$  then  $V_{rca}[j] \leftarrow V_{rca}[i];$ 
                else if  $V_{rca}[i] = 0$  and  $V_{rca}[j] > 0$  then  $V_{rca}[i] \leftarrow V_{rca}[j];$ 
                else if  $V_{rca}[i] > 0$  and  $V_{rca}[j] > 0$  then ( $V_{rca} = V_{rca}[i]$ )  $\leftarrow V_{rca}[j];$ 
                else
                     $n_{rca} \leftarrow n_{rca} + 1;$ 
                     $V_{rca}[i] \leftarrow n_{rca};$ 
                     $V_{rca}[j] \leftarrow n_{rca};$ 
                end
            end
        end
    end
end

```

Algorithm 5: The Recursive Cluster Algorithm. Decomposes a list of vortices into vortex dipoles or clusters. Vortices are labelled with a cluster number, with vortex dipoles labeled with -1 .

3.3.2 Ripley's K function

$$K(x) = \frac{A}{n^2} \sum_{i \neq j} I(d_{ij} < x), \quad (3.1)$$

where d_{ij} is the distance between the i th and j th points, A is the area of the region containing every point, n is the number of points, x is the search radius, and I is the indicator function (1 if its argument is true, 0 otherwise). Should the points be distributed homogeneously in space, then $K(s) \approx \pi s^2$.

3.4 Tracking vortex trajectories

3.5 Removing vortices with phase unwrapping

```

input : A  $n_x \times n_y$  complex field  $\psi$ . A 'safe' distance  $d$ . Vortex core radius  $c$ .
output: A  $n_x \times n_y$  complex field  $\phi$ .

 $\phi \leftarrow \psi;$ 
 $(n_v, V_l, V_p) \leftarrow \text{Algorithm 4} \leftarrow \psi;$ 
for  $i \leftarrow 1$  to  $n_v$  do
    if  $|V_l[i]| > d$  then
        Imprint a vortex of polarity  $V_p[i]$  at location  $V_l[i]$  in  $\phi$ ;
        for  $j \leftarrow -c$  to  $c$  do
            for  $k \leftarrow -c$  to  $c$  do
                 $x \leftarrow V_l[1, i] + j;$ 
                 $y \leftarrow V_l[2, i] + k;$ 
                 $\phi(x, y) \leftarrow \psi_{\text{inf}} \times \text{phase}(\psi(x, y));$ 
            end
        end
    end
end

```

Algorithm 6: The 'vortex killer' algorithm. By accurately imprinting a vortex, this algorithm removes vortices from the input wavefunction non destructively.

Part III

Numerical Studies

Chapter 4

Vortex deflection

4.1 Comparison of deflection from a vortex and an impurity

4.2 Special Cases

Chapter 5

Classical-like wakes behind elliptical obstacles in Bose-Einstein condensates

When citing references the main commands to use are `\citet` and `\citep`.

- `\citet` is used for a textual citation, e.g. it was shown by Allen et al. [1] that...
- `\citep` is used for a parenthetical citation, e.g. there has been much work done in this area [see, for example, 1, 2]...

See the full Natbib documentation for more detailed usage instructions.

Theorem 5.1. *This is how you write a theorem ...*

Proof. ...with its associated proof. □

Lemma 5.1. *You can also have lemmas ...*

Corollary 5.1. ...or corollaries ...

Proposition 5.1. ...or propositions.

Definition. Definitions are not numbered by default, but you can change this in the thesis style file `inputs/masthesis.sty`.

Example. Similarly for examples ...

Remark. ...and remarks.

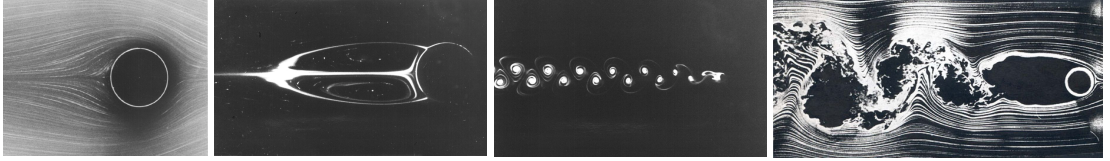


Figure 5.1: Classical viscous flow past a cylinder. From left to right: laminar flow ($Re = 3.64$) [3]; steady symmetric wake behind the cylinder ($Re = 41$) [3]; time-dependent Bénard–von Kármán vortex street ($Re = 112$) [4]; and chaotic downstream wake ($Re > 10^5$) [5].

5.1 Introduction

Recent experimental [6, 7], numerical [8, 9, 10] and theoretical studies [11] have highlighted similarities between turbulence in quantum fluids (e.g. superfluid helium and atomic Bose-Einstein condensates) and turbulence in ordinary (classical) fluids [12]. In particular, it is found that, in the idealized case of homogeneous isotropic conditions away from boundaries, the distribution of kinetic energy over the length scales obeys the celebrated Kolmogorov scaling of classical turbulence [13]. This similarity is remarkable, because a superfluid has zero viscosity and vorticity is not a continuous field but is concentrated in discrete vortex filaments of fixed circulation κ proportional to Planck's constant. In the more realistic presence of boundaries (such as an obstacle or confining channel walls), superfluid hydrodynamics is less understood, despite the large number of experiments in such scenarios.

In a classical viscous fluid [12], the prototype problem with a boundary is the flow around a cylinder or a sphere (or, changing the frame of reference, the motion of a cylinder or a sphere in a fluid at rest). The nature of such flow is determined by the Reynolds number $Re = vd/\nu$, where v is the (assumed uniform) flow's velocity away from the obstacle, d is the obstacle's size, and ν is the fluid's kinematic viscosity. If $Re \lesssim 50$, a steady symmetric wake forms behind the obstacle; if $10^2 \lesssim Re \lesssim 10^5$ the wake becomes asymmetric and time dependent, forming the famous Bénard–von Kármán vortex street structure. These cases are depicted in Figure 5.1. At even higher Re , the flow becomes turbulent.

What happens in a superfluid is not clear. Firstly, the superfluid has zero viscosity ($\nu = 0$) and hence Re cannot be defined. Secondly, experiments performed in superfluid helium confirm that the flow is affected by the boundaries [14, 15]; unfortunately what is observed is not the flow pattern itself, but rather the trajectories of tracer particles, whose relation with the flow is still the subject of investigations [16]. Numerical simulations of three-dimensional (3D) superfluid flow around an oscillating sphere performed using the vortex filament model were not conclusive - quantum vortices did not appear to organise themselves into a visible classical-like wake near the obstacle [17, 18, 19].

The two-dimensional (2D) scenario of an obstacle moving through a superfluid offers a simplified platform to consolidate analogs and disparities between classical and quantum

fluids. In their pioneering simulations of the 2D nonlinear Schrödinger equation, Frisch and Pomeau [20] observed the formation of vortex pairs in the flow past a circular obstacle. A more complete picture has been recently revealed by Sasaki *et al.* [21]. Below a critical velocity (which depends on the strength [22] and shape of the external potential), the fluid undergoes laminar flow around the obstacle. Above this critical velocity vortices become nucleated and peel off from the moving obstacle. Two patterns are possible, depending on the size of the obstacle: vortex-antivortex pairs in either a symmetric [20] or asymmetric configuration (with the preference for the latter); or alternating pairs of like-signed vortices, forming a trail analogous to the Bernárd-von Kármán vortex street. At higher velocities, vortex nucleation becomes highly irregular. Recent studies of this 2D system have considered vortex emission and drag [23, 24, 25, 26], the critical velocity [27, 28, 29, 30, 31], the effect of inhomogeneous potentials [25, 32, 33], the role on the obstacle parameters [26, 34], and supersonic effects such as oblique dark solitons [35] and Cerenkov radiation [36].

In this work we present the first clear evidence of a classical wake in superfluid flow past an obstacle. Using the Gross-Pitaevskii equation (GPE) for a zero-temperature Bose-Einstein condensate and an elliptical obstacle, we show that the interaction of discrete vortex singularities downstream of the obstacle yields a flow pattern which indeed mimics classical vortex flow.

5.2 Model

We consider an atomic Bose-Einstein condensate (BEC) moving relative to a laser-induced obstacle (imposed through an external potential), as realized experimentally in 3D [37, 38, 39, 2] and quasi-2D condensates [2]. This scenario closely resembles that of the classical wake-problem [3, 4]. On a much larger scale, a similar 3D configuration has been experimentally realized in liquid helium [14, 15].

The BEC, assumed to be weakly-interacting and at ultracold temperature, is parameterized by its mean-field wavefunction $\Psi(\mathbf{r}, t)$, which defines the fluid number density $n(\mathbf{r}, t) = |\Psi|^2$. The wavefunction satisfies the non-linear Schrödinger equation, also known as the Gross-Pitaevskii equation [40], where a cubic nonlinearity arises from the mean-field potential generated by the dominant *s*-wave (contact) atom-atom interactions. The equation is,

$$i\hbar \frac{\partial \Psi}{\partial t} = \left(-\frac{\hbar^2}{2m} \nabla^2 + V(\mathbf{r}, t) + g|\Psi|^2 - \mu \right) \Psi. \quad (5.1)$$

Here $g = 4\pi\hbar^2 a_s/m$ is the interaction coefficient, with a_s being the atomic *s*-wave scattering length and m the atomic mass, and μ is the chemical potential of the condensate. The GPE is solved in the reference frame moving with the obstacle, at speed v along x .

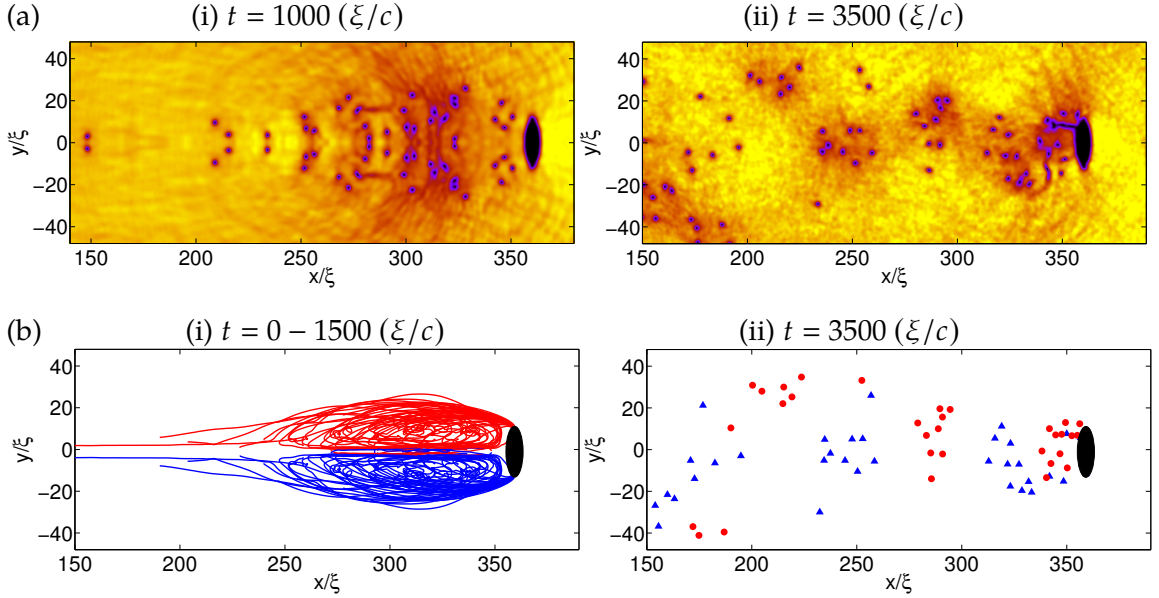


Figure 5.2: Snapshots showing the (a) density profile and (b) vortex trajectories during vortex shedding from an elliptical object ($\epsilon = 3$) at (i) early times and (ii) later times. The obstacle has speed $v = 0.52c$ and size $d = 5\xi$. Red and blue lines represent vortices of oppositely quantized circulation. At early t , a symmetric wake similar to a classical fluid with low Re forms. Symmetry breaks at $t \approx 1500 (\xi/c)$ at which point vortex motion becomes disordered. In this case the initial condition is noise-free.

The external potential acting on the system $V(\mathbf{r}, t)$ is taken to be zero everywhere, i.e. a homogeneous system with uniform density n_0 , apart from a localized repulsive potential, Gaussian in shape, which represents the obstacle. A key feature of this work is that the obstacle is taken to be elliptical, of ellipticity ϵ , with the short axis being parallel to the flow, x . Such a potential, in its 2D form, can be generated via the repulsive optical dipole force from an incident blue-detuned laser beam which is moved relative to the condensate either by deflection of the beam [37, 38, 39] or motion of the condensate itself when offset in a harmonic trap [2]. While laser-induced obstacles generated to date have had a circular profile, elliptical modification of the Gaussian potential can be achieved via cylindrical focussing of the laser beam.

We express length in terms of the healing length $\xi = \hbar/\sqrt{mn_0g}$, speed in terms of the speed of sound $c = \sqrt{n_0g/m}$, and time in terms of (ξ/c) . A detailed description of the model can be found in Appendix A.

5.3 Results: Two-Dimensional Wakes

We begin by exploring quantum wakes in the 2D flow of a BEC past an obstacle, according to the 2D GPE with the elliptical potential defined in Equation (5.5).

5.3.1 Vortex emission from elliptical obstacles

For illustrative purposes we first consider an elliptical obstacle (size $d = 5\xi$, ellipticity $\epsilon = 3$) moving at speed $v = 0.365c$. This speed exceeds the critical velocity for the obstacle such that quantum vortices become nucleated and trail behind to form a wake [Figure 5.2(a)]. Sound waves, also generated by the obstacle, have little effect on the vortex dynamics. At early times [Figure 5.2(a)(i)], the vortex shedding occurs through the symmetric generation of vortex-antivortex pairs, leading to a collimated and symmetric wake behind the obstacle. This is in qualitative agreement with observations for circular obstacles [20, 23, 25, 26], although, for the same obstacle velocity and size, the elliptical obstacle induces a higher frequency of vortex emission and thus a denser wake. We examine the role of ellipticity in more detail in Sections 5.3.3 and 5.3.4.

At later times [Figure 5.2(a)(ii)], the flow becomes asymmetric due to the known instability of symmetric wakes [23]. A striking pattern emerges whereby distinct clusters of co-rotating vortices (of the order of 5 vortices in each cluster) develop downstream of the obstacle. Each cluster contains vortices of the same sign and adjacent clusters have alternating sign. These clusters form a Bénard–von Kármán vortex street downstream from the obstacle, confirming the intuition that a sufficiently large number of quanta of circulation reproduce classical physics. Here, the ellipticity of the obstacle facilitates the formation of this street; the relatively high rate of vortex emission leads to a greater interaction between vortices in the wake which in turn promotes clustering. In contrast, for a circular obstacle the symmetric wake evolves into a V-shaped wake of vortex-antivortex pairs [21]; this because the vortex emission rate and hence their subsequent interaction is insufficient to induce significant clustering.

The vortex trajectories provide visualisation of the time-integrated nature of the wake [Figure 5.2(b)]. At early times (i), we see that the vortex trajectories are symmetric, forming a flow pattern in striking analog to the classical wake at low Re . The generic development of vortex trajectories is as follows. Pairs of singly-quantized vortices of opposite sign peel off from the poles of the obstacle and interact with each other as vortex-antivortex pairs. Each pair propagates in the positive x direction with approximate velocity $\hbar/(md_p)$ [21], where d_p is the pair separation [41]; the pair's velocity is less than the obstacle's velocity and it drifts behind the obstacle. As the pair moves further away from the obstacle, its separation decreases and its velocity increases, such that it begins to catch the obstacle up. Once the pair is sufficiently close to the obstacle, it again separates and slows down, then the cycle repeats. As more vortices are nucleated, two distinct clusters of like-circulation form. Nucleated pairs then travel around the outside of the existing cluster before contracting, speeding up and travelling through the middle of the clusters towards the obstacle. The clusters grow until they reach a maximum size depending on the obstacle's size and speed. Hereafter, nucleated vortex pairs travel around the outside of the two clusters and

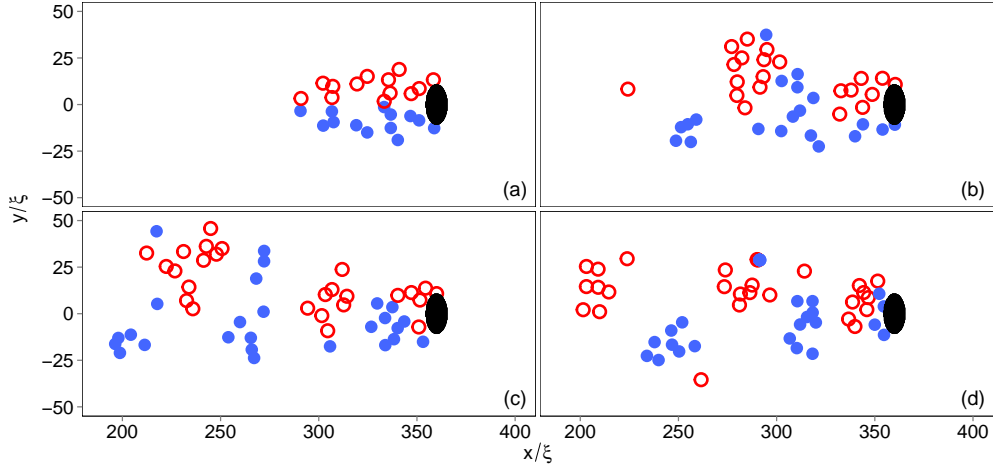


Figure 5.3: Snapshots of vortex locations during the motion of an elliptical object ($d = 5\xi$ and $\varepsilon = 3$) at speed $v = 0.52c$ in the presence of small-amplitude noise at $t = 0$. The snapshots are at times (a) $t = 450$, (b) 900 , (c) 1000 and (d) 1100 (ξ/c). Red/blue circles represent vortices with quanta of circulation $+1/-1$. The wake forms into clusters of like-circulation that continue to be produced, in analogy to the classical Bénard–von Kármán vortex street from a cylinder.

continue travelling downstream, becoming lost from the main wake.

5.3.2 Formation of the Bénard–von Kármán vortex street

Once the symmetry of the wake is broken, vortices no longer separate into two distinct clusters of like-circulation. Existing vortices and newly-nucleated vortices mix together behind the obstacle. However it is apparent in Figure 5.2(b)(ii) that, on average, positive vortices drift to $y > 0$ while negative vortices prefer to drift to $y < 0$.

To accelerate the formation of the asymmetric wake, we subsequently seed the initial condition with noise. Figure 5.3 shows the vortex locations at various stages of the evolution. The initial symmetry of the wake [Figure 5.3(a)] breaks at $t \approx 450(\xi/c)$, with the wake splitting into several clusters. The velocity field around the obstacle is affected: it depends on time and the distance of the nearest cluster of vortices. The obstacle no longer simultaneously produces vortex-antivortex pairs, but now generates a series of like-signed vortices. Since like-signed vortices are known to co-rotate, these vortices group into clusters which slowly rotate. This cluster effects the velocity field once more, causing a cluster of opposite signed vortices to be produced. This process then repeats such that clusters of like signed vortices are then produced behind the obstacle, much like vorticity in the classical vortex street behind a cylinder. While some positive clusters contain negative vortices and vice versa, the overall pattern is still a time-dependent Bénard–von Kármán vortex street.

For clusters consisting of pairs of vortices, it has been shown that they can survive

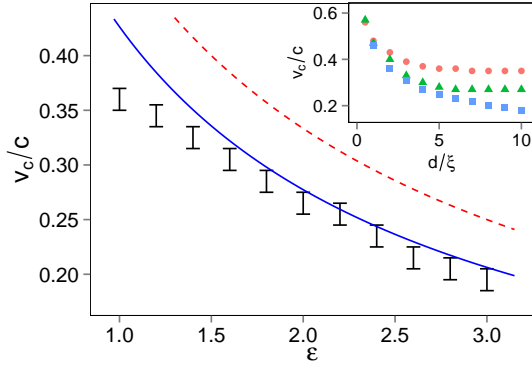


Figure 5.4: Critical velocity against obstacle ellipticity ε , for $d = 10\xi$. Shown are the results from the numerical simulations (black bars), Equation (5.2) (dashed red line) and Equation (5.3) (solid blue line). Inset: Critical velocity (obtained numerically) versus the obstacle width d , for ellipticities $\varepsilon = 1$ (red circles), $\varepsilon = 2$ (green triangles) and $\varepsilon = 3$ (blue squares).

downstream for a very long time [21]. However, for regimes with larger numbers of vortices in each cluster, the chaotic nature of vortex motion can cause originally tightly packed and circular clusters to easily stretch over large areas, form strange shapes, or even split into smaller clusters. Examples of this will be shown later in Figure 5.5.

5.3.3 Critical Velocity past an Elliptical Obstacle

Elliptical obstacles facilitate the formation of semi-classical wakes because they reduce the critical velocity and enhance the vortex shedding frequency. Figure 5.4(a) shows the critical velocity for flow past the obstacle as a function of its ellipticity, taking the obstacle to have fixed width in the y -direction of $d = 10\xi$. We determine the critical velocity numerically by performing simulations with flow velocities increasing in steps of 0.01 until vortices nucleate. For a circular object, we find that the critical velocity is $v_c = 0.355(\pm 0.005)c$, consistent with predictions in the Eulerian ($d \gg \xi$) limit [29, 30, 31]. As the ellipticity is increased (i.e. the obstacle becomes narrower in x), the critical velocity decreases. The modification of the critical velocity is significant: if $\varepsilon = 3$, v_c is more than 40% smaller than that for a circular obstacle.

The rough dependence of v_c on ε can be derived as follows. According to Landau's criterion [42], superfluidity breaks down when the fluid velocity exceeds the critical velocity $v_{\text{Lan}} = \min[E(p)/p]$, where p is the momentum of elementary excitations and $E(p)$ their energy. The weakly-interacting Bose gas has the dispersion relation $E(p) = [ngp^2/m + p^4/(4m^2)]^{1/2}$, hence $v_{\text{Lan}} = c$. If an obstacle moves through the fluid with speed v , the local fluid velocity at the poles exceeds v . Approximating the BEC as an inviscid Euler fluid undergoing potential flow about the object, then the maximum local velocity

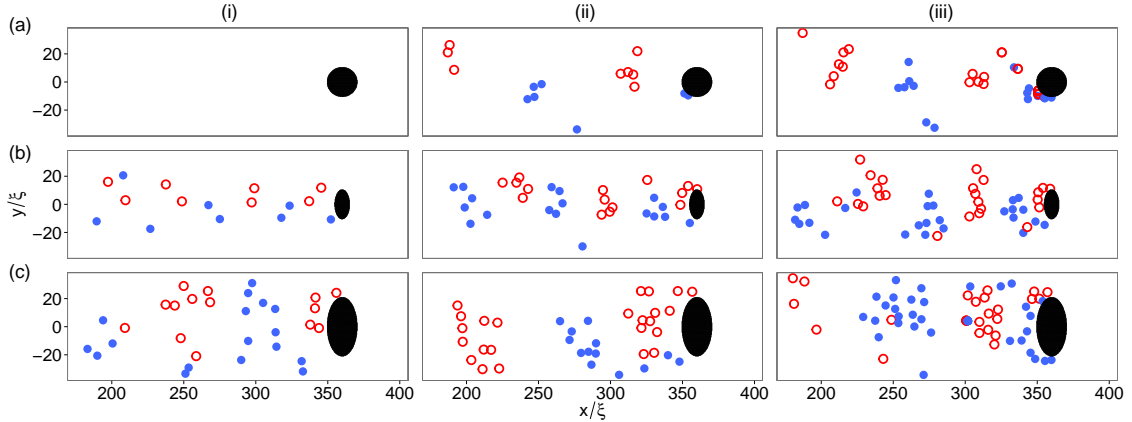


Figure 5.5: Snapshots of the vortex positions for various obstacle parameters, at $t = 2000$ (ξ/c). Shown are obstacles corresponding to (a) $\varepsilon = 1$ and $d = 5\xi$, (b) $\varepsilon = 2$ and $d = 5\xi$, and (c) $\varepsilon = 2$ and $d = 10\xi$, at the velocities (i) $v = 0.32c$, (ii) $v = 0.40c$, and (iii) $v = 0.48c$. Red/blue circles represent vortices with quanta of circulation $+1/-1$.

is $v_{\max} = (1 + \varepsilon)v$ and the Landau critical velocity is (dashed red line in Figure 5.4(a)),

$$\frac{v_{c1}}{c} = \frac{1}{1 + \varepsilon}. \quad (5.2)$$

While this result assumes constant density, a first order correction can be made by using Bernoulli's theorem to model the reduction in local density near the obstacle (due to the enhanced local fluid velocity) which in turn reduces the local speed of sound $c(x, y) = \sqrt{n(x, y)g/m}$ [43]. This then leads to the modified result,

$$\frac{v_{c2}}{c} = \left[\frac{3}{2}(1 + \varepsilon)^2 - \frac{1}{2} \right]^{-\frac{1}{2}}. \quad (5.3)$$

This relation (solid blue line in Figure 5.4) gives good agreement with the computed values of v_c . The deviation for $\varepsilon \sim 1$ has been noted elsewhere [30], and can be remedied using higher order corrections.

From studies on circular objects, it is known that v_c depends on the obstacle's shape at small diameters, where boundary layer effects are significant; v_c approaches the "Eulerian" value only for large diameters $d \gg \xi$ [26, 30]. The variation of v_c with the obstacle width d is shown in Figure 5.4 (inset). For $d = 10\xi$, the critical velocity effectively reaches its asymptotic value, while at smaller widths, it is much larger.

5.3.4 Role of Obstacle Size and Ellipticity on the Wake

During the initial symmetric phase of vortex nucleation, the wakes generated by the obstacle have the same qualitative structure shown in Figure 5.2(b) (i). However, once the wake

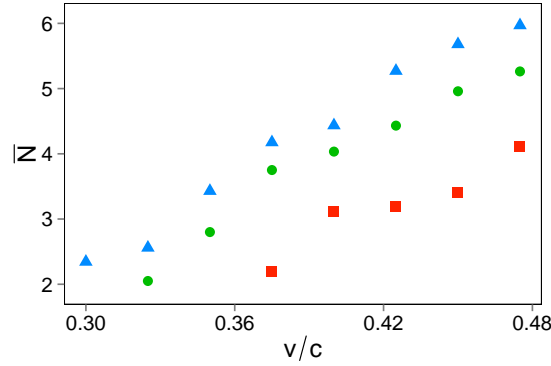


Figure 5.6: Average number of vortices in the clusters as a function of the obstacle velocity v . Shown are cases with $\varepsilon = 1$ (red squares), $\varepsilon = 2$ (green circles) and $\varepsilon = 3$ (blue triangles). All cases feature $d = 5\xi$.

becomes asymmetric, the nature of the clusters that form are highly dependent on the velocity and shape of the obstacle. Figure 5.5 shows wakes generated for various obstacle parameters, all captured at the same time $t = 2000 (\xi/c)$. We find that any increase of size, ellipticity or velocity of the obstacle increases the number of vortices in the wake's clusters.

The shedding frequency of vortices increases with the velocity of the flow [24]. For an elliptical obstacle, the combination of a reduced critical velocity and increased local velocity around the obstacle has the effect of increasing the shedding frequency with ε and d . The overall result is that, when increasing any of v , ε or d , more vortices are nucleated in a given time period, causing the cluster size to increase. This increase in cluster size is investigated in the next section.

5.3.5 Vortex Clustering

We have shown that the Bénard–von Kármán vortex street forms through the clustering of like-signed vortices. Methods of quantifying the clustering of vortices in quantum fluids have been explored in the literature [44, 45, 46]. Here we utilize the algorithm of Reeves *et. al.* [45] to identify clusters.

Firstly we record the number of clusters N_c and the number of vortices in each cluster N_i , where i is the cluster index. Then we determine the average number of vortices in the clusters, $\bar{N} = (1/N_c) \sum_{i=1}^{i=N_c} N_i$ as a function of obstacle velocity v for three ellipticities $\varepsilon = 1, 2$ and 3 , at times $t = 500(\xi/c), 510(\xi/c), \dots, 2500(\xi/c)$. The results, plotted in Figure 5.6, show that increasing v (above the critical velocity) causes \bar{N} to increase and that, at fixed v , \bar{N} increases with ε . We attribute this to an object with a larger ε having a lower critical velocity and producing more vortices at the same v . This result explains why an elliptical obstacle efficiently generates a semi-classical wake composed of large vortex clusters. We also find that for all values of ε , a large obstacle velocity ($v \gtrsim 0.6$) causes

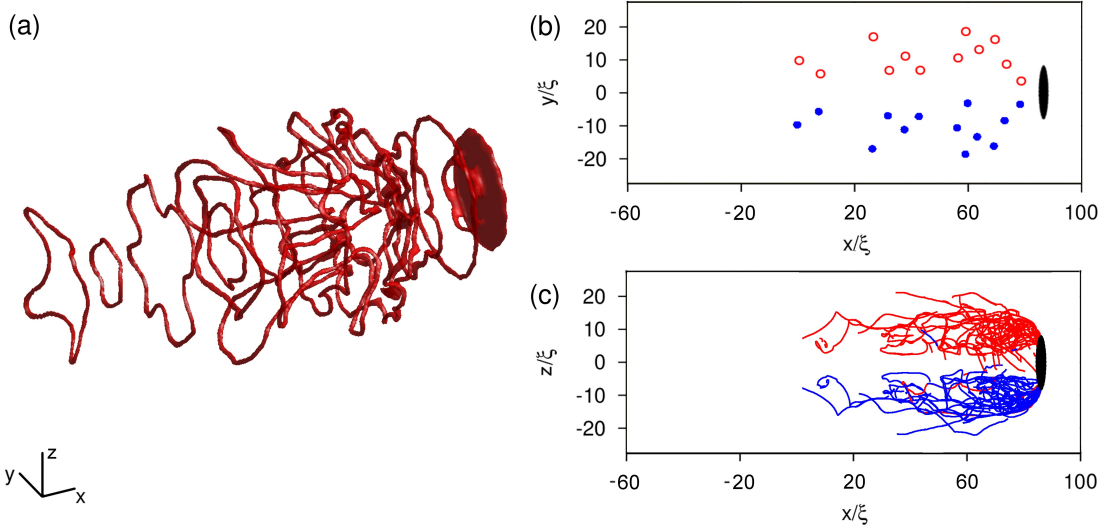


Figure 5.7: Symmetric wake in 3D at $t = 450$ (ξ/c) for an elliptical obstacle ($d = 5\xi$ and $\epsilon = 5$) moving at $v = 0.6c$. (a) Isosurface plot of low density, over a range $[0, 100]$ in x and $[-25, 25]$ in y and z . (b) Vortex locations in the xy plane. (c) Vortex trajectories in the xz plane. Here (b) and (c) show opposing circulation in red and blue.

vortices to nucleate non-periodically, inducing an irregular flow without a visible Bénard-von Kármán vortex street configuration, in agreement with previous simulations with circular obstacles of smaller diameter [21].

5.4 Results: Three-Dimensional Wakes

We now generalize our results to 3D by considering quantum wakes in three-dimensional flow past a localized obstacle, as simulated via the 3D GPE with the 3D obstacle potential of Equation (5.4). Our results will confirm that the features observed in 2D wakes also arise in the 3D setting. A comprehensive study of the parameter space is, however, not tractable in 3D due to the computational intensity of the 3D simulations.

5.4.1 Symmetric Wakes

For a spherical ($\epsilon = 1$) object with $d = 5\xi$, we find that the critical velocity is $v_c = 0.455 \pm 0.05c$, consistent with $v_c = 0.55c$ reported in the Eulerian limit ($d \gg \xi$) [43, 47]. Making the obstacle ellipsoidal, with the short direction parallel to the flow, reduces the critical velocity, in parallel with our 2D observations. For example, for $\epsilon = 5$, the critical velocity is reduced to $v_c = 0.315 \pm 0.05c$. Figure 5.7(a) shows the 3D wake generated past this ellipsoidal obstacle ($d = 5\xi$ and $\epsilon = 5$) when moving at super-critical speed $v = 0.6c$. Vortex rings, the 3D analog of vortex-antivortex pairs, are ejected at high frequency (due to the obstacles high ellipticity) in the direction of the flow. At early times ($t = 450$ (ξ/c)

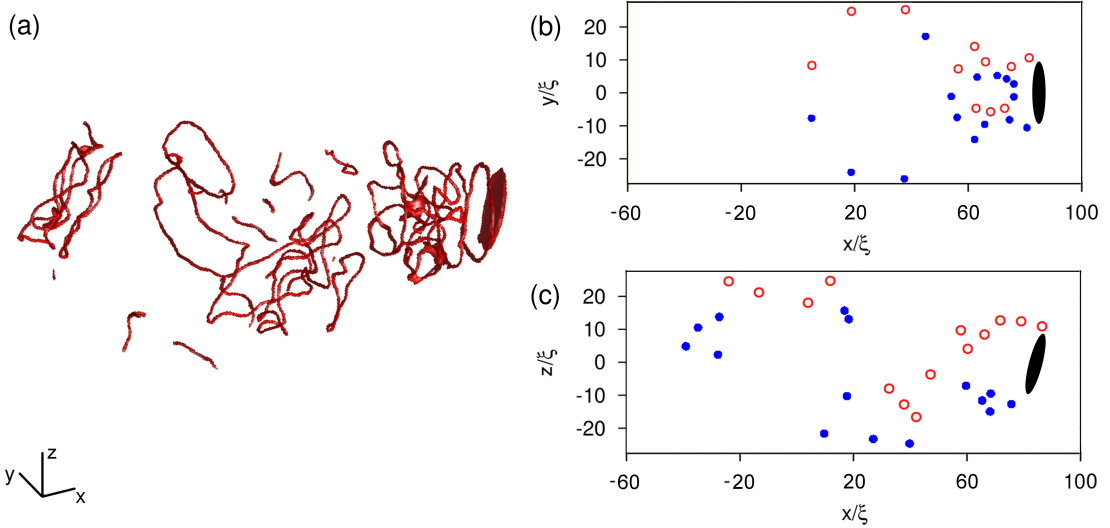


Figure 5.8: Asymmetric wake in 3D at $t = 340$ (ξ/c) for an elliptical obstacle ($d = 5\xi$ and $\epsilon = 5$) moving at $v = 0.6c$. (a) Isosurface plot of low density, over a range $[-60, 100]$ in x and $[-25, 25]$ in y and z . (b) Vortex locations in the xy plane. (c) Vortex locations in the xz plane. Here (b) and (c) show opposing circulation in red and blue.

in this case) the vortex configuration maintains cylindrical symmetry about the obstacle's axis, as is clearly visible in the xy and xz planes in Figure 5.7(b) and (c). As the vortex rings move downstream they shrink and speed up, returning to the object, sometimes passing through other vortex rings. A similar behaviour is observed [48] in the evolution of toroidal bundles of many coaxial vortex rings which leapfrog around each other. Occasionally a ring will escape this cycle and fall downstream. These behaviors conspire to form an organized symmetric wake behind the obstacle, the 3D analog of our 2D observations.

5.4.2 Asymmetric Wakes

We break the cylindrical symmetry of the system by tilting the obstacle by a small angle in the xz plane. The vortex rings, illustrated in Figure 5.8, now become ejected and evolve asymmetrically; Kelvin waves and reconnections occur, forming an apparently disordered tangle of vortices behind the obstacle. Due to the manner in which symmetry is broken, the wake remains approximately symmetric in the xy plane, as evident in Figure 5.8 (b). However, unlike in Figure 5.8, the vortices do not self organise into two clusters of alternate circulation. This is due to the vortex rings interacting, reconnecting and shifting out of the plane (which manifests in 2D as two alternate-sign vortices approaching one another).

However, in the xz plane (Figure 5.8 (c)), symmetry is broken. Due to the relatively high frequency of vortex nucleation and relatively low flow speed, like signed vortices cluster together as they are ejected by the obstacle, much like the 2D solutions seen in earlier sections. Downstream the tangle may shift both across or out of the plane. In 2D,

although this manifests as a shift in location of the vortex clusters, the clusters largely remain rather than forming dipoles.

5.5 Conclusion

We have shown that the motion of an obstacle in a Bose-Einstein condensate produces classical-like wakes consisting of quantum vortices of the same polarity. This is consistently observed in both two- and three-dimensional scenarios. The key ingredient to produce classical-like wakes - that vortices are generated at a sufficiently high rate that they undergo strong interactions with their neighbours (rather than being swept away) - is that the obstacle is elliptical, which reduces the critical velocity for vortex nucleation. Symmetric wakes resemble those observed in classical flow at low Re . These are unstable, forming time-dependent asymmetric structures similar to the Bénard–von Kármán vortex street of classical fluid dynamics. Vortex singularities in the inviscid superfluid thus mimic classical vortex patterns typical of viscous flows. The effects which we describe (dependence of the critical velocity and cluster size on the obstacle's size, velocity and ellipticity) can be experimentally studied in atomic Bose-Einstein condensates using moving laser-induced potentials. They are also relevant to the motion of objects (such as vibrating wires, grids and forks) in superfluid helium, as the obstacle's ellipticity plays a role which is analogous to rough boundaries [49, 50].

5.6 Model of 2D and 3D BEC with Gaussian Potentials

In our 3D simulations, we solve the 3D GPE of Equation (1), where the localized 3D obstacle is modelled via a repulsive ellipsoidal Gaussian potential,

$$V(\mathbf{r}, t) = V_0 \exp\left(-\frac{\varepsilon^2(x - x_0 - vt)^2}{d^2} - \frac{(y - y_0)^2}{d^2} - \frac{(z - z_0)^2}{d^2}\right), \quad (5.4)$$

where V_0 is its (constant) amplitude, d its width in the y and z directions, and (x_0, y_0, z_0) its initial coordinates. The GPE is transformed into the reference frame moving with the obstacle (in x) via the addition of the Galilean term $i\hbar v \frac{\partial}{\partial x} \Psi$ to the right-hand side of the GPE (5.1), where v is the frame velocity.

To effectively reduce the system to two-dimensions, the BEC is assumed to be confined by a harmonic trapping potential in the axial (z) direction, $V(z) = \frac{1}{2}m\omega_z^2 z^2$, where m is the atomic mass. For sufficiently strong trapping, which requires $\hbar\omega_z \gg \mu$, where μ is the chemical potential of the 3D condensate, the axial wavefunction becomes “frozen” into the time-independent harmonic oscillator ground state $\pi^{-1/4} l_z^{-1/2} \exp(-z^2/2l_z^2)$, where $l_z =$

$\sqrt{\hbar/m\omega_z}$ is the axial harmonic oscillator length. Under these conditions, the condensate becomes effectively two-dimensional, as achieved experimentally [51]. It is then described by an 2D GPE, corresponding to Equation (5.1) with $g \rightarrow g/2\pi l_z^2$ and where Ψ , \mathbf{r} , V and n become two-dimensional quantities.

In 2D, we model the obstacle via a moving repulsive Gaussian potential of the form,

$$V(\mathbf{r}, t) = V_0 \exp\left(-\frac{\varepsilon^2(x - x_0 - vt)^2}{d^2} - \frac{(y - y_0)^2}{d^2}\right). \quad (5.5)$$

The 3D (2D) system is simulated using the 4th-order Runge-Kutta method under periodic boundary conditions on a $400 \times 150 \times 150$ (2048×512) grid with uniform spacing $\Delta = 0.4\xi$. The obstacle is positioned upstream in the box to enable a long simulation time before vortices recycle through the periodic box. We have verified that our simulations are well-converged, that is, increasing the grid resolution has negligible effect on the results. The computational box is sufficiently large that the boundary conditions do not play a role in vortex shedding. The initial condition is the stationary state of the GPE (including obstacle potential) with $v = 0$ (as determined by the imaginary time convergence method). Setting $V_0 = 100 \mu$ throughout, the external potential closely approximates an impenetrable obstacle. Unless stated otherwise, a small amount of noise is added to the initial condition to break symmetry: a random number between -0.0005 and 0.0005 is added to both the real and imaginary parts of the initial wavefunction.

To minimize initial generation of waves, v is ramped up in time along a hyperbolic tangent curve, from $v = 0$ at $t = 0$ to its terminal value at around $t \approx 100$ (ξ/c). During the evolution, the vortices are located (and their circulation evaluated) using an algorithm based on those of references [52] and [44].

Chapter 6

Decay of 2D quantum turbulence in a highly oblate Bose-Einstein condensate

6.1 Introduction

Ultracold gaseous Bose-Einstein condensates (BECs) provide a unique testbed with which to investigate the phenomenon of quantum turbulence and the more rudimentary realm of superfluid vortex dynamics [53, 54]. These systems provide an impressive degree of parameter manipulation unavailable in superfluid helium, the traditional context for studying quantum turbulence [55], with scope to control the particle interactions and potential landscape in both time and space. The typical size of these systems is only one or two orders of magnitude larger than the inter-vortex spacing, which in turn is another order of magnitude larger than the vortex core size. These compact length scales mean that the collective behaviour of vortices and their interaction with the background condensate is significant. The emergence of turbulent-like behaviour in the form of a vortex tangle was observed by Henn *et al.* in 2009 by oscillating a three-dimensional condensate [?]. What's more, the experimentalist's handle over the confining potential enables crossover to two-dimensional quantum turbulence [56]: by tightly confining the trap geometry along one axis, such that the vortices closely embody point vortices [57], states of two-dimensional quantum turbulence have been recently reported [58, 59].

In the recent experiment of Kwon *et al.* [59], a trapped, oblate BEC was translated past a stationary, laser-induced obstacle. As is characteristic of superfluids, vortices and anti-vortices were nucleated into the condensate once the relative speed exceeded a critical value [20]. A state of two-dimensional quantum turbulence emerged, characterized by a disordered distribution of vortices. The authors monitored the number of vortices, reveal-

ing the dependence on the relative speed and the thermal relaxation of the vortices. They directly observed vortex collision events, characterized by a crescent-shaped depletion in the condensate density. Furthermore, some vortex cores were seen to coalesce, evidence of vortex pair annihilation.

In this article we elucidate these experimental findings through mean-field simulations of the two-dimensional (2D) Gross-Pitaevskii equation (GPE), both at zero-temperature and in the presence of thermal dissipation, modelled through a phenomenological dissipation term in the GPE. Notably, our simulations provide insight into the sign of the circulation of the vortices and the early-stage evolution, not accessible experimentally. We establish the key stages of the dynamics, from the initial nucleation of vortices and formation of a quasi-classical wake, through the rapid symmetry breaking and disorganization of the vortices, to the decay of the vortices by annihilation or passage out of the condensate. Our approach gives excellent agreement with the experimental observations.

6.2 Set-Up

In the experiment, a ^{23}Na condensate with $N = 1.8 \times 10^6$ atoms was confined within a highly-oblate cylindrically symmetric harmonic trap $V_{\text{trap}}(x, y, z) = \frac{1}{2}m[\omega_r^2(x^2+y^2)+\omega_z^2z^2]$, with axial frequency $\omega_z = 2\pi \times 350$ Hz and radial frequency $\omega_r = 2\pi \times 15$ Hz (corresponding to an aspect ratio parameter $\omega_z/\omega_r \approx 23$) and where m denotes the atomic mass. A 2D mean-field description is strictly valid when the condition $Nal_z^3/l_r^3 \ll 1$ is satisfied, where $l_z = \sqrt{\hbar/m\omega_z}$ and $l_r = \sqrt{\hbar/m\omega_r}$ are the axial and radial harmonic oscillator lengths and a is the s -wave scattering length [60, 61]. For this experiment, $Nal_z^3/l_r^3 = 8.3$, i.e. the system remains 3D in nature. Nonetheless, the dynamics of the vortices is essentially 2D because of the suppression of Kelvin waves in the z -direction [62]. Therefore, we will adopt a 2D description throughout this work and show that it is sufficient to capture the experimental observations. It is worth noting that in the xy plane the condensate closely approximates a Thomas-Fermi (inverted parabola) density profile with radius $R_{\text{TF}} \approx 70\mu\text{m}$.

We parameterize the condensate by a 2D wavefunction $\phi(x, y, t)$; the condensate density distribution follows as $n(x, y, t) = |\phi(x, y, t)|^2$. The wavefunction satisfies the 2D GPE:

$$i\hbar \frac{\partial \phi}{\partial t} = \left(-\frac{\hbar^2}{2m} \nabla^2 + V(x, y, t) + g|\phi|^2 - \mu \right) \phi \quad (6.1)$$

where μ denotes the chemical potential of the condensate and $g = 2\hbar a(2\pi\omega_z\hbar/m)^{1/2}$ characterizes the effective 2D nonlinear interactions arising from s -wave atomic collisions. We solve the GPE on a 1024×1024 grid using a fourth-order Runge-Kutta method. The vortex core size is characterized by the healing length $\xi = \hbar/\sqrt{mg}$; at the condensate centre this has the value $\xi \approx 0.6\mu\text{m}$. The grid spacing is $0.27\mu\text{m}$ in both x and y , and we have verified

that reducing the grid spacing has no effect on our results.

Following the experiment, the total potential acting on the condensate $V(x, y, t)$ is the above harmonic trap plus a static Gaussian-shaped obstacle potential $V_{\text{obs}}(x, y) = V_0 \exp[-2(x^2 + y^2)/d^2]$, located at the origin, with $V_0 = 15\mu$ and $d = 15\mu\text{m}$. The initial ground-state BEC is obtained by solving the GPE in imaginary time with enforced norm $N = 1.8 \times 10^6$. At $t = 0$ the harmonic trap is centered at $x = 18.5\mu\text{m}$. The trap is translated towards the left, at speed v , over a distance of $37\mu\text{m}$; to smooth this speed curve we additionally include a linear acceleration/deceleration over 3.75ms at the start/end, which is included as part of the $37\mu\text{m}$ translation. Once the trap is at rest, the obstacle amplitude V_0 is ramped down to zero over 0.4s.

6.3 Results

6.3.1 Number of Vortices Generated

Following removal of the obstacle, we determine the number of vortices in the system N_v (performed by identifying locations where the condensate possesses a 2π singularity in the phase). We limit our search to 75 percent of the Thomas-Fermi radius (centred on the centre-of-mass to account for sloshing motion); by avoiding the low density periphery we avoid artifacts from ghost vortices and match closely what is performed experimentally (since vortices close to the edge are not detected due to low signal-to-noise [63]). In Fig. 6.1 we plot N_v versus the translation speed v . We see the same *qualitative* form between our simulations (red circles) and the experiment (black crosses): above a critical speed $v_c \approx 0.45\text{mm/s}$ vortices enter the system, nucleated by the relative motion between the obstacle and the superfluid, and for $v > v_c$ the growth in N_v is initially rapid but tails off for $v \gg v_c$. Quantitatively, however, the GPE overestimates N_v . One can expect that thermal dissipation, not accounted for in the GPE, will act to reduce the number of vortices in the system. We introduce the effects of such dissipation via the addition of phenomenological dissipation, γ [64, 65], which enters the GPE (6.1) by replacing i on the left hand side by $(i - \gamma)$. This term induces the decay of excitations; for single vortices this manifests in them spiraling out of the trapped condensate [66, 62, 1, 67]. We choose a small value $\gamma = 0.0003$ so as to model the experiment in its very coldest realization of $\sim 130\text{nK}$ and enforce the norm throughout the dissipative simulations so as to emulate the experiment (for which no significant loss of atom number was observed).

With this dissipation the data for N_v becomes reduced, bringing it closely in line with the experimental data. Experimental limitations in resolving and counting vortices may also contribute to the over-estimate of N_v from the GPE.

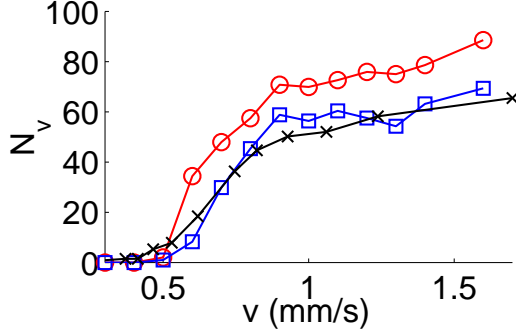


Figure 6.1: (Color online) Number of vortices N_v in the condensate after removal of the obstacle. Shown are simulations of the GPE without dissipation (red circles), with dissipation $\gamma = 0.0003$ (blue squares) and experimental results extracted from Fig. 1 of [59] (black crosses). Each point is averaged over 20 ms once the obstacle amplitude reaches $V_0 = 0$. For comparison, the speed of sound in the center of the BEC is $v_c \approx 4.6$ mm/s.

6.3.2 Stages of the Condensate Evolution

We now examine in detail the evolution of the condensate, charting its dynamics from the initial stage (when the harmonic trap translation begins) to the intermediate and final stages (randomization and decay of the vortices). We see the same qualitative evolution with and without dissipation, and for all velocities exceeding v_c . For the purposes of illustration, we focus on an example with dissipation and a translation speed $v = 1.4$ mm/s.

Figure 6.2 shows the condensate density at various times. At the start of the simulation ($t = 0$) the condensate has a smooth circular density profile, with a density depression due to the obstacle. Later vortices appear as small dots of low density; superimposed red/blue markers tag vortices of positive/negative circulation.

Vortex Nucleation and Wake Formation

To initiate the dynamics, the harmonic trap is translated to the left. This is performed sufficiently rapidly that the condensate does not adiabatically follow the trap minimum, but rather begins a sloshing motion in the trap; the centre-of-mass of the BEC oscillates at the trap frequency and the BEC undergoes a quadrupolar shape oscillation. As the BEC sloshes first to the left, its speed increases. When the local fluid velocity exceeds the speed of sound [20], vortices nucleate at the poles of the obstacle (where the local fluid velocity is the greatest) and are washed downstream (to the left). The pattern of vortices nucleated by a moving obstacle in a superfluid depends, in general, on the speed, shape and size of the obstacle [22? , 68]. During the initial evolution vortices of negative and positive circulation are created near each pole in an irregular manner, sometimes with alternating circulation; other times several vortices of the same circulation appear. In our case, the rate of vortex nucleation is sufficiently high that the vortices interact strongly with each other, collectively forming macroscopic clusters of negative and positive vortices downstream of the object ($t = 43$ ms). This is reminiscent of the wakes in classical viscous fluids past cylindrical obstacles [68]. During this early stage, vortices of opposite circulation may become very close and annihilate (i.e. undergo a 2D reconnection), leaving behind density

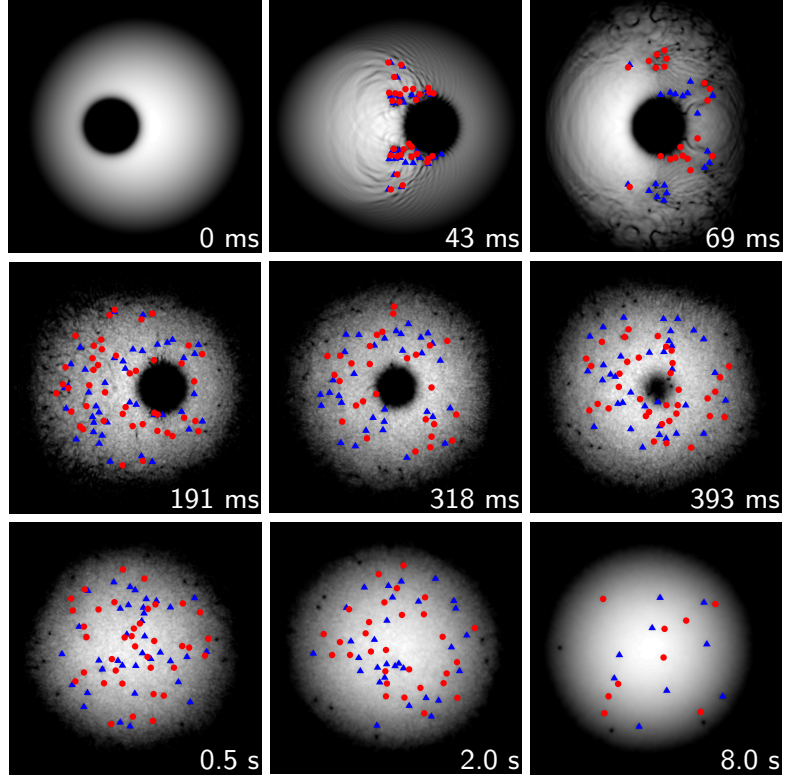


Figure 6.2: (Color online) Snapshots of the condensate density, for a translational speed $v = 1.4\text{mm/s}$ and in the presence of dissipation ($\gamma = 0.0003$). The obstacle is completely removed at 0.43s. The field of view in each subfigure is of size $[170\mu\text{m}]^2$ and shifted along the x -axis so as to best display the condensate. Vortices with positive (negative) circulation are highlighted by red circles (blue triangles).

(sound) waves. The condensate then sloshes to the right; this motion not only carries the existing vortices to the opposite (right) side of the obstacle but nucleates further vortices. As the condensate's sloshing mode is damped by the dissipation, the relative speed of the obstacle decreases and the vortex nucleation pattern changes: like-signed vortices are generated near each pole, forming symmetric classical-like wakes [68]. This effect leads to further clustering of like-signed vortices ($t = 69\text{ms}$). As the condensate continues to slosh, more vortices nucleate into the system. It must be stressed that, up to these early times ($t = 191\text{ms}$), the vortex distribution remains symmetric about the x axis. Without the dissipation term in the GPE, the sloshing mode initially decays while the obstacle is present but then persists with constant amplitude once the obstacle is removed. If dissipation is included then the sloshing mode continues to decay.

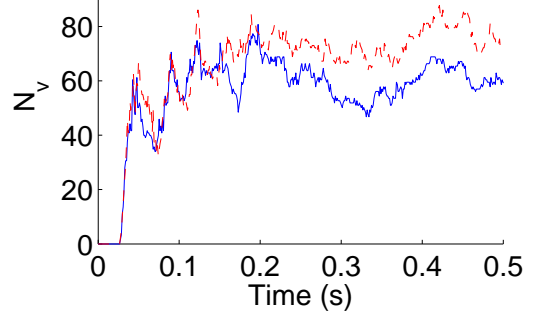


Figure 6.3: Growth of vortex number (in a single realization) at early times for a translational speed of $v = 1.4\text{mm/s}$. Shown are the results with no dissipation (red dashed line) and with dissipation $\gamma = 0.0003$ (blue solid line).

Vortex Randomization

In the presence of the obstacle and the sloshing mode, vortices continually nucleate and their spatial distribution remains approximately symmetric about the x axis. At later times ($t > 318\text{ms}$) this symmetry breaks and the vortices evolve into a completely disorganized, apparently random configuration with no significant clustering of like-signed vortices. This random distribution of vortices is consistent with the experimental observations [59]; following this we also classify the system as one of quantum turbulence. Besides vortices, the condensate contains also collective modes and an energetic, disordered sound field, with this spatial range of excitations further indicative of two-dimensional quantum turbulence [56, 58]. (Note that the typical characteristic diagnostics of steady-state 2D quantum turbulence, e.g. power-law energy spectra and the inverse energy cascade, are not appropriate here since the system is not continuously driven and does not reach steady state.)

The vortex randomization is driven by the growth of numerical noise. We have repeated our results in the presence of imposed noise (amplitude 5%, as described elsewhere [68]) and find the qualitative dynamics to be unchanged (although, as one would expect, the vortex randomization occurs at a slightly earlier time). This noise serves to model the natural fluctuations that arises in a realistic experimental scenario, e.g. due to thermal and quantum atomic fluctuations, electromagnetic noise, vibrations, etc.

It is interesting to note the obstacle is still in the system at this point, nucleating vortices in a symmetrical manner. The disorganized vortices already in the system create a velocity field which quickly mixes newly created vortices nucleated at the poles of the obstacle. Visual inspection, confirmed by a clustering-detection algorithm [44, 45], shows no significant clusters beyond this stage of the evolution. By the time the obstacle is removed the vortex configuration is essentially random, but the number of positive and negative vortices stays approximately equal. It is important to remark that, without detecting the sign of the vortex circulation, we could not reach these conclusions.

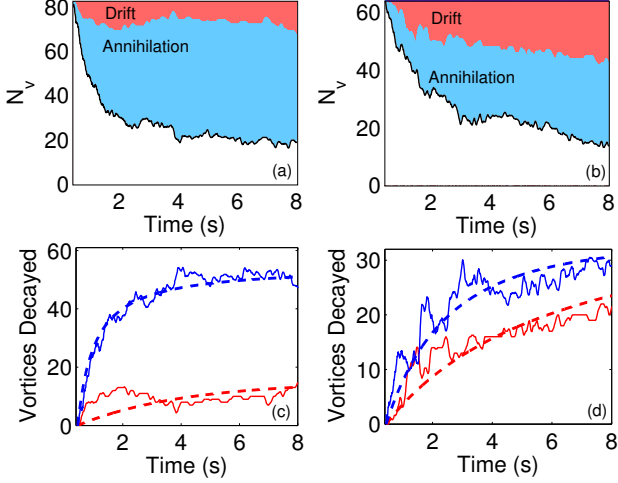


Figure 6.4: Vortex decay in the absence of dissipation (a, c) and with dissipation $\gamma = 0.0003$ (b, d) for a translational speed of $v = 1.4\text{mm/s}$. The upper figures show the decay of the total vortex number $N_v(t)$, with the contribution of drifting and annihilation depicted by the shaded regions. The lower figures show the drift number $N_d(t)$ and annihilation number $N_a(t)$, plus their respective fits.

Vortex Decay

It is clear from Fig. 6.2 that, following the removal of the obstacle, the number of vortices (N_v) depletes. Indeed, one expects that the condensate will decay towards its vortex-free, time-independent ground state. To quantify the vortex generation and decay, Fig. 6.3 plots N_v versus time. The onset of vortex nucleation is at around $t = 0.02\text{ms}$; this is the time taken for accelerating condensate to exceed the speed of sound at the poles of the object. At first N_v grows steeply, as vortices (around 40-60) are rapidly driven into the system. Subsequently, N_v grows more slowly; vortices continue to be nucleated from the obstacle but vortices undergo annihilation or move into low density regions where they are not detected. The fluctuations in N_v are amplified, particularly at early times, by the shape oscillations of the condensate, which carry vortices in and out of the detection radius. As the obstacle is removed at $t \approx 0.4\text{s}$, the surrounding condensate fills the low density area. Vortices (including some outside of the detection radius) move inwards with the flow, causing N_v to peak.

Following removal of the obstacle, the vortex number N_v decays with time. This is shown in Fig. 6.4(a) and (b) for the absence and presence of dissipation, respectively. Kwon *et al.* [59] argued that there are two mechanisms by which vortices decay: (i) thermal dissipation (resulting in drifting of vortices to the edge of the condensate), and (ii) vortex-antivortex annihilation events, and proposed that the vortex decay takes the form:

$$\frac{dN_v}{dt} = -\Gamma_1 N_v - \Gamma_2 N_v^2. \quad (6.2)$$

Here the linear and nonlinear terms, parameterized by the positive coefficients Γ_1 and Γ_2 , respectively, model these two decay processes. From our simulations we are able to independently count the number of vortices which drift out and the number which annihilate. We decompose the number of vortices according to $N_v(t) = N_{v0} - N_d(t) - N_a(t)$,

where N_{v0} is the initial number of vortices (when the obstacle is removed), $N_d(t)$ is the cumulative number of vortices which have drifted out of the condensate and $N_a(t)$ is the cumulative number which have undergone pair annihilation. The contribution of both vortex drifting and annihilation to the overall decay of N_v is depicted by the coloured regions in Fig. 6.4(a) and (b). In the absence of dissipation the vortex decay is dominated by annihilation. Indeed, apart from at early times (where internal condensate dynamics carry vortices out to high radii), no vortices drift out. In contrast, in the presence of dissipation, vortices continue to drift out over time, consistent with dissipative dynamics of single vortices [1].

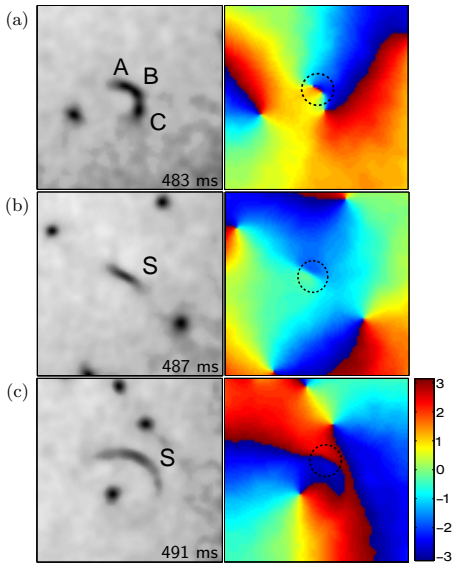


Figure 6.5: Density (left) and phase (right) just before (a), immediately following (b) and a later time after (c) a vortex-antivortex annihilation event. The field of view is $[23.5\mu\text{m}]^2$, centered on the vortex pair/sound pulse (highlighted by a circle in the phase).

6.3.3 Crescent-Shaped Density Structures

In the experiment, Kwon *et al.* observed the occasional appearance of crescent-shaped waves of depleted density. Lacking direct access to the vortex signs, they suggested that these structures result from annihilation events of vortices of opposite circulation [69, 70, 71]: a vortex reconnection is predicted to induce an intense, localised, rarefaction sound pulse [72, 73]. Figure 6.5 shows snapshots of the condensate density and phase during a reconnection event. Vortices show up as localized dips in the density (left column) and 2π -defects in the phase (right column). Figure 6.5 (a) shows a vortex (A) and antivortex (B) close to each other, and a third vortex (C) in the vicinity. Note that the individual vortices are not spatially resolvable through their density alone (the vortex cores merge into a deep, elongated crescent-shaped depression), but they are clearly identified by the phase plot. A short time later (b), vortices A and B annihilate, as confirmed by the disappearance

Our decomposition of N_v enables us to independently fit the drift and annihilation decay processes (as two coupled ODEs for N_d and N_a , equivalent to Eq. (6.2)), with the results shown in Fig. 6.4(c) and (d). In the absence of dissipation, we find $\Gamma_2 = 0.0040$ (It is not appropriate to discuss Γ_1 since $N_d(t)$ is not of a decaying form). While the experimental observations [59] suggest Γ_2 is proportional to T^2 and thus approaches 0 as $T \rightarrow 0$, our results demonstrate a finite Γ_2 in this limit. In the presence of dissipation we obtain $\Gamma_1 = 0.093$ and $\Gamma_2 = 0.0041$, which are comparable to the coldest experiments of Kwon *et al.*

of their phase singularities, leaving behind a shallow rarefaction pulse (S) with a linear phase step. This pulse rapidly evolves into a shallow, crescent-shaped sound wave [Fig. 6.5 (c)]. In other words, our simulations yield crescent-shaped density features as seen in the experiment, but these features are not uniquely formed by annihilation events - they may also result from two (or more) vortices in close proximity. Information about the condensate phase is thus crucial to distinguish the nature of these observed structures. In this direction, an approach has recently been proposed for the experimental detection of quantized vortices and their circulation in a 2D BEC [74].

6.3.4 Vortex Generation via an Elliptical Obstacle

It is evident from the snapshots in Figure 2 that the initial translation of the condensate past the obstacle generates not just vortices but also shape excitations, sound waves (low-amplitude density waves), and high-amplitude density waves. These additional excitations will heat the condensate and modify the subsequent turbulent dynamics in a highly nonlinear and complicated manner. While reducing the translational speed reduces this disruption, this also reduces the number of vortices. A less disruptive and more efficient (higher rate of vortex nucleation) means to generate vortices may be provided by employing a laser-induced obstacle with *elliptical*, rather than circular, cross-section (attainable through cylindrical beam focusing). Repeating our simulations with such an elliptical obstacle $V_{\text{obs}}(x, y) = V_0 \exp [-2(\epsilon^2 x^2 + y^2)/d^2]$ with arbitrary ellipticity $\epsilon = 3$ (the short/long axis being parallel/perpendicular to the flow) confirms the same qualitative behaviour as for homogeneous systems [68]: the ellipticity acts to reduce the critical superfluid velocity and, for a given flow speed, increase the rate of vortex nucleation. To illustrate the merits of the elliptical obstacle, in Fig. 6 we depict snapshots of the condensate dynamics for ellipticity $\epsilon = 3$ and a translational speed of $v = 0.8\text{mm/s}$. Despite a lower translational speed, the number of vortices generated by the time the obstacle is removed is almost identical to the circular example of Fig. 3. As a consequence of the reduced translational speed, the condensate disruption is visibly reduced. It is also worth noting that the elliptical obstacle promotes the formation of clusters of like-signed vortices (see intermediate time), and thus may facilitate future exploration of coherent vortex structures.

6.4 Conclusion

In conclusion, we have shown that the recent experimental creation and decay of vortices within a BEC [59] is well described by simulations of the 2D GPE with phenomenological dissipation (despite the 3D nature of the system). Theoretical access to the condensate phase, and thus the circulation of the vortices, promotes our understanding of the dynamics. In the early stages of translation of the obstacle, a quasi-classical wake of vortices

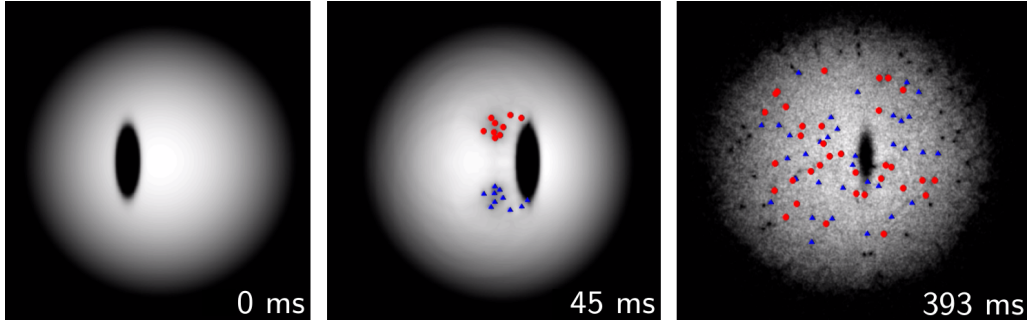


Figure 6.6: (Color online) Snapshots of the condensate density for a translational speed $v = 0.8\text{mm/s}$ past an elliptical obstacle (ellipticity $\epsilon = 3$). The field of view in each subfigure is of size $[170\mu\text{m}]^2$ and shifted along the x -axis so as to best display the condensate. Compared to the corresponding snapshots in Figure 2, the elliptical obstacle generates as many final vortices but at a lower translational speed and with reduced condensate disruption.

forms behind it, before symmetry breaking causes disorganisation of the vortices. After the obstacle is removed, the vortices decay in a manner which is both qualitatively and quantitatively consistent with the two mechanisms proposed by Kwon *et al.*, i.e. loss of vortices at the condensate edge due to thermal dissipation and vortex-antivortex annihilation events within the condensate. We confirm the occasional appearance of crescent-shaped density features, resulting either from the proximity of vortex cores or from a sound pulse which follows a vortex-antivortex reconnection. Finally, we propose that a moving *elliptical* obstacle may provide a cleaner and more efficient means to generate two-dimensional quantum turbulence.

Chapter 7

Critical velocity at finite temperature

7.1 Strongly Non-equilibrium initial condition

7.2 Vortex shedding

7.3 Critical velocity for vortex production

Chapter 8

Simulating the surface of a “Floppy Wire”

- 8.1 Superfluid wire experiments**
- 8.2 The “Floppy Wire” AFM image**
- 8.3 GPE with AFM surface**
- 8.4 2D clusters and backflow vortex generation**
- 8.5 3D boundary layer and velocity statistics**

Appendix A

Detailed Derivations

A.1 Derivation of the Hydrodynamic Equations via the Madelung Transformation

Inserting the Madelung transformation (Section 2.6) into the GPE and writing the result in tensor notation yields

$$i\hbar \left(\frac{\partial R}{\partial t} + i \frac{\partial \theta}{\partial t} R \right) e^{i\theta} = -\frac{\hbar^2}{2m} e^{i\theta} \left(\frac{\partial^2 R}{\partial x_j^2} + 2i \frac{\partial \theta}{\partial x_j} \frac{\partial R}{\partial x_j} + i \frac{\partial^2 \theta}{\partial x_j^2} R - \frac{\partial \theta}{\partial x_j} \frac{\partial \theta}{\partial x_j} R \right) + gR^3 e^{i\theta} + VR e^{i\theta}.$$

The real and imaginary parts of the GPE, once divided by $\exp(i\theta)$, then take the form

$$-\hbar R \frac{\partial \theta}{\partial t} = -\frac{\hbar^2}{2m} \left(\frac{\partial^2 R}{\partial x_j \partial x_j} - R \frac{\partial \theta}{\partial x_j} \frac{\partial \theta}{\partial x_j} \right) + gR^3 + VR, \quad (\text{A.1})$$

$$\hbar \frac{\partial R}{\partial t} = -\frac{\hbar^2}{2m} \left(2 \frac{\partial \theta}{\partial x_j} \frac{\partial R}{\partial x_j} + R \frac{\partial^2 \theta}{\partial x_j \partial x_j} \right). \quad (\text{A.2})$$

Consider Equation (A.2) and note that $\rho = mR^2 \Rightarrow \frac{\partial \rho}{\partial t} = 2mR \frac{\partial R}{\partial t}$, allowing us to rewrite the equation in terms of ρ ,

$$\begin{aligned} \frac{\partial \rho}{\partial t} &= -\hbar R \left(2 \frac{\partial \theta}{\partial x_j} \frac{\partial R}{\partial x_j} + R \frac{\partial^2 \theta}{\partial x_j \partial x_j} \right) \\ &= -2mR \frac{\partial R}{\partial x_j} \frac{\partial}{\partial x_j} \left(\frac{\hbar}{m} \theta \right) - mR^2 \frac{\partial^2}{\partial x_j \partial x_j} \left(\frac{\hbar}{m} \theta \right) \\ &= -\frac{\partial \rho}{\partial x_j} \frac{\partial}{\partial x_j} \left(\frac{\hbar}{m} \theta \right) - \rho \frac{\partial^2}{\partial x_j \partial x_j} \left(\frac{\hbar}{m} \theta \right). \end{aligned}$$

The terms containing the phase can then be directly replaced with the fluid velocity, $v_j = \frac{\partial}{\partial x_j} \left(\frac{\hbar}{m} \theta \right)$.

$$\begin{aligned}\frac{\partial \rho}{\partial t} &= -\frac{\partial \rho}{\partial x_j} v_j - \rho \frac{\partial}{\partial x_j} v_j \\ &= -\frac{\partial}{\partial x_j} (\rho v_j).\end{aligned}$$

Rewritten in vector form the result is a continuity equation,

$$\frac{\partial \rho}{\partial t} + \nabla(\rho \mathbf{v}) = 0. \quad (\text{A.3})$$

Now consider Equation (A.1), written in the form

$$\frac{\hbar}{m} \frac{\partial \theta}{\partial t} = \frac{\hbar^2}{2m^2} \left(\frac{1}{R} \frac{\partial^2 R}{\partial x_j \partial x_j} - \frac{\partial \theta}{\partial x_j} \frac{\partial \theta}{\partial x_j} \right) - \frac{gR^2}{m} - \frac{V}{m}.$$

Note that it can easily be shown $\frac{1}{R} \frac{\partial^2 R}{\partial x_j \partial x_j} = \frac{1}{\sqrt{\rho}} \nabla^2 \sqrt{\rho}$ and $\frac{\hbar^2}{2m^2} \frac{\partial \theta}{\partial x_j} \frac{\partial \theta}{\partial x_j} = \frac{v^2}{2}$. It follows that Equation (A.1) can be written,

$$\begin{aligned}\frac{\hbar}{m} \frac{\partial \theta}{\partial t} &= \frac{\hbar^2}{2m^2} \frac{1}{\sqrt{\rho}} \nabla^2 \sqrt{\rho} - \frac{v^2}{2} - \frac{gR^2}{m} - \frac{V}{m} \\ \Rightarrow \frac{\partial}{\partial t} \left(\frac{\hbar}{m} \frac{\partial \theta}{\partial x_k} \right) &= \frac{\partial}{\partial x_k} \left(\frac{\hbar^2}{2m^2} \frac{1}{\sqrt{\rho}} \nabla^2 \sqrt{\rho} \right) - \frac{\partial}{\partial x_k} \left(\frac{v^2}{2} \right) - \frac{2gR}{m} \frac{\partial R}{\partial x_k} - \frac{1}{m} \frac{\partial V}{\partial x_k} \\ \Rightarrow \rho \frac{\partial v_k}{\partial t} &= \rho \frac{\partial}{\partial x_k} \left(\frac{\hbar^2}{2m^2} \frac{1}{\sqrt{\rho}} \nabla^2 \sqrt{\rho} \right) - \rho \frac{\partial}{\partial x_k} \left(\frac{v^2}{2} \right) - 2gR^3 \frac{\partial R}{\partial x_k} - \rho \frac{1}{m} \frac{\partial V}{\partial x_k}.\end{aligned}$$

By noticing that $p = \frac{1}{2} g \left(\frac{\rho}{m} \right)^2 = \frac{gR^4}{2}$ we can write $\frac{\partial p}{\partial x_k} = 2gR^3 \frac{\partial R}{\partial x_k}$ and then,

$$\rho \frac{\partial v_k}{\partial t} + \rho \frac{\partial}{\partial x_k} \left(\frac{v^2}{2} \right) = \rho \frac{\partial}{\partial x_k} \left(\frac{\hbar^2}{2m^2} \frac{1}{\sqrt{\rho}} \nabla^2 \sqrt{\rho} \right) - \frac{\partial p}{\partial x_k} - mR^2 \frac{\partial}{\partial x_k} \left(\frac{V}{m} \right).$$

We now now use the following two results,

$$\begin{aligned}v_j \frac{\partial}{\partial x_j} v_k &= \frac{\partial}{\partial x_k} \left(\frac{v_j v_k}{2} \right) \\ 2 \frac{\partial}{\partial x_k} \left(\frac{1}{\sqrt{\rho}} \frac{\partial^2}{\partial x_j \partial x_j} \sqrt{\rho} \right) &= \frac{1}{\rho} \frac{\partial}{\partial x_j} \rho \frac{\partial}{\partial x_j} \frac{\partial}{\partial x_k} \ln \rho,\end{aligned}$$

and find,

$$\rho \left(\frac{\partial}{\partial t} v_k v_j \frac{\partial v_k}{\partial x_j} \right) = -\frac{\partial p}{\partial x_k} - \frac{\partial}{\partial x_j} P_{jk} - \rho \frac{\partial}{\partial x_k} \left(\frac{V}{m} \right),$$

where $P_{jk} = -\frac{\hbar^2}{4m^2} \rho \frac{\partial^2 \ln \rho}{\partial x_j \partial x_k}$. Writing this in vector notation, we obtain an equation similar to the Euler equation for an inviscid fluid,

$$\rho \left(\frac{\partial \mathbf{v}}{\partial t} + (\mathbf{v} \cdot \nabla) \mathbf{v} \right) = -\nabla p - \nabla \mathbf{P} - \rho \nabla \left(\frac{V}{m} \right). \quad (\text{A.4})$$

A.2 Derivation of the Gross-Pitaevskii Equation through Quantum Field Theory

This section derives the GPE following the methodology outlined in [NPP GPE tutorial]. We begin by revisiting the quantum field theory formalism used to describe a many body quantum system[Fetter 71]. Such a system is described by an N-body wavefunction, $\tilde{\Psi}(\mathbf{r}_1 \dots \mathbf{r}_N, t)$ which obeys the famous Schrödinger equation

$$i\hbar \frac{\partial}{\partial t} \tilde{\Psi}(\mathbf{r}_1 \dots \mathbf{r}_N, t) = \hat{H} \tilde{\Psi}(\mathbf{r}_1 \dots \mathbf{r}_N, t), \quad (\text{A.5})$$

where \mathbf{r}_i describes the coordinates of the i th body. Now consider a closed system containing a dilute, weakly interacting Bose gas of N atoms. Such a system would be described by $\tilde{\Psi}(\mathbf{r}_1 \dots \mathbf{r}_N, t)$, with a Hamiltonian of the form

$$\hat{H} = \sum_{k=1}^N \hat{h}_0(\mathbf{r}_k, t) + \frac{1}{2} \sum_{k,l=1}^N \hat{V}(\mathbf{r}_k, \mathbf{r}_l). \quad (\text{A.6})$$

Here $\hat{h}_0(\mathbf{r}_k, t) = -\frac{\hbar^2}{2m} \nabla^2 + V_{\text{ext}}(\mathbf{r}, t)$ is a contribution arising from the effects of a single particle in an external potential. We assume in the dilute gas all interactions are binary; and so the second term arises from collisions between 2 atoms only. The factor of $\frac{1}{2}$ ensures the effects are only counted once over the entire sum.

We now reformulate this system in a different representation, using the so called ‘occupation number’ orthonormal basis $|n_1 \dots n_\infty\rangle$. This basis arises from the observation that multiple particles sharing an energetically accessible state are indistinguishable. Instead we consider only the number of particles in each state i and denote this n_i . Such states often correspond to states with fixed energy ε_i . While the number of states are infinite, our system contains a fixed number of bosons, N , implying that there are at most N states occupied.

The wavefunction is mapped into the ‘occupation number’ basis via

$$\tilde{\Psi}(\mathbf{r}_1 \dots \mathbf{r}_N, t) \rightarrow |\tilde{\Psi}(t)\rangle = \sum_{n_1 \dots n_\infty} c(n_1 \dots n_\infty, t) |n_1 \dots n_\infty\rangle,$$

with $c(n_1 \dots n_\infty, t)$, appropriately chosen complex coefficients. The values c must follow the

particle statistics rules (e.g. for Bosons must be symmetric under swapping of quantum numbers) and be normalised so that the probabilities correctly sum to one. For our bosons this leads to the

$$\int |\tilde{\Psi}|^2 d\mathbf{r} = 1 \Rightarrow \sum_{n_1 \dots n_\infty} |c(n_1 \dots n_\infty, t)|^2 \frac{N!}{n_1! \dots n_\infty!} = 1.$$

In this formulation, note that the state vectors $|n_1 \dots n_\infty\rangle$ are time-independent, and the evolution of the system is entirely encoded in the values of $c(n_1 \dots n_\infty, t)$. As part of the overall picture, we also must describe the movement of bosons between different states or energy levels. It is convenient to visualise the simultaneous destruction of a particle in state j and creation of a particle in state i , described mathematically using the single particle annihilation and creation operators[Shiff49].

$$\hat{a}_j |n_1 \dots n_i \dots n_j \dots n_\infty\rangle = \sqrt{n_j} |n_1 \dots n_i \dots n_j - 1 \dots n_\infty\rangle,$$

$$\hat{a}_i^\dagger |n_1 \dots n_i \dots n_j \dots n_\infty\rangle = \sqrt{n_i + 1} |n_1 \dots n_i + 1 \dots n_j \dots n_\infty\rangle,$$

which satisfy the bosonic commutation relations,

$$[\hat{a}_i, \hat{a}_j^\dagger] = \delta_{ij} \quad [\hat{a}_i, \hat{a}_j] = [\hat{a}_i^\dagger, \hat{a}_j^\dagger] = 0.$$

Any single particle changing states can now be described through these operators. A particle moving from state j to state i can be described using a single annihilation operator and a single creation operator, through the product $\hat{a}_i^\dagger \hat{a}_j$. Similarly, as we decided to simplify the system by considering a dilute gas where all interactions are binary collisions, all interactions can be described by two particles changing state, using the product $\hat{a}_i^\dagger \hat{a}_k^\dagger \hat{a}_j \hat{a}_l$. Using these tools and ideas, the original description in Equations A.5 and A.6 is now written

$$i\hbar \frac{\partial}{\partial t} |\tilde{\Psi}\rangle = \hat{H} |\tilde{\Psi}\rangle,$$

with the Hamiltonian

$$\hat{H} = \sum_{ij} \langle i | \hat{h}_0 | j \rangle \hat{a}_i^\dagger \hat{a}_j + \frac{1}{2} \sum_{ijkl} \langle ik | \hat{V} | jl \rangle \hat{a}_i^\dagger \hat{a}_k^\dagger \hat{a}_j \hat{a}_l, \tag{A.7}$$

where

$$\begin{aligned}\langle i | \hat{h}_0 | j \rangle &= \int \phi_i^*(\mathbf{r}) \hat{h}_0 \phi_j(\mathbf{r}) d\mathbf{r}, \\ \langle ik | \hat{V} | jl \rangle &= \frac{1}{2} [(ik| \hat{V} | jl) + (ik| \hat{V} | lj)], \\ \langle ik | \hat{V} | jl \rangle &= \iint \phi_i^*(\mathbf{r}) \phi_k^*(\mathbf{r}') \hat{V}(\mathbf{r} - \mathbf{r}') \phi_l(\mathbf{r}') \phi_j(\mathbf{r}) d\mathbf{r}' d\mathbf{r}.\end{aligned}$$

For further convenience we introduce the so called Bose field operators

$$\begin{aligned}\hat{\Psi}(\mathbf{r}, t) &= \sum_i \hat{a}_i(t) \phi_i(\mathbf{r}, t), \\ \hat{\Psi}^\dagger(\mathbf{r}, t) &= \sum_i \hat{a}_i^\dagger(t) \phi_i(\mathbf{r}, t),\end{aligned}$$

which can be thought of as operators that represent the addition or removal of a particle at time t and location \mathbf{r} . As with the annihilation and creation operators, the Bose field operators also satisfy the commutation relations,

$$[\hat{\Psi}(\mathbf{r}, t), \hat{\Psi}^\dagger(\mathbf{r}', t)] = \delta(\mathbf{r} - \mathbf{r}') \quad [\hat{\Psi}(\mathbf{r}, t), \hat{\Psi}(\mathbf{r}', t)] = [\hat{\Psi}^\dagger(\mathbf{r}, t), \hat{\Psi}^\dagger(\mathbf{r}', t)] = 0. \quad (\text{A.8})$$

Using these operators, the Hamiltonian in Equation A.7 can be again rewritten as

$$\begin{aligned}\hat{H} &= \int \hat{\Psi}^\dagger(\mathbf{r}, t) \hat{h}_0 \hat{\Psi}(\mathbf{r}, t) d\mathbf{r} \\ &\quad + \frac{1}{2} \iint \hat{\Psi}^\dagger(\mathbf{r}, t) \hat{\Psi}^\dagger(\mathbf{r}', t) V(\mathbf{r} - \mathbf{r}') \hat{\Psi}(\mathbf{r}', t) \hat{\Psi}(\mathbf{r}, t) d\mathbf{r}' d\mathbf{r}.\end{aligned} \quad (\text{A.9})$$

where, as before, $\hat{h}_0(\mathbf{r}_k, t) = -\frac{\hbar^2}{2m} \nabla^2 + V_{\text{ext}}(\mathbf{r}, t)$ and $V(\mathbf{r} - \mathbf{r}')$ is the two body interaction potential.

One of our original assumptions about the Bose gas was the fact it was weakly interacting with only binary collisions. We now add to this approximation a frequent simplification of the interaction potential so that all interactions are considered totally elastic contact collisions. The strength of this interaction is usually taken to be $g = 4\pi\hbar^2/a$, where a is the s-wave scattering length, measured for a particular atom in the lab. Our two body interaction potential then becomes,

$$V(\mathbf{r} - \mathbf{r}') = g \delta(\mathbf{r} - \mathbf{r}'),$$

which when inserted into Equation A.9 gives the Hamiltonian,

$$\hat{H} = \int \hat{\Psi}^\dagger(\mathbf{r}, t) \hat{h}_0 \hat{\Psi}(\mathbf{r}, t) d\mathbf{r} + \frac{g}{2} \int \hat{\Psi}^\dagger(\mathbf{r}, t) \hat{\Psi}^\dagger(\mathbf{r}, t) \hat{\Psi}(\mathbf{r}, t) \hat{\Psi}(\mathbf{r}, t) d\mathbf{r}.$$

The Bose field operator $\hat{\Psi}(\mathbf{r}, t)$ evolves over time according to the Heisenberg equation of motion

$$i\hbar \frac{\partial}{\partial t} \hat{\Psi}(\mathbf{r}, t) = [\hat{\Psi}(\mathbf{r}, t), \hat{H}].$$

By expanding out the commutator, using standard commutator identities along with the relations in Equation A.8 and integrating out resulting delta functions we find

$$\begin{aligned} i\hbar \frac{\partial}{\partial t} \hat{\Psi}(\mathbf{r}, t) &= \int [\hat{\Psi}, \hat{\Psi}^\dagger \hat{h}_0 \hat{\Psi}] d\mathbf{r} + \frac{g}{2} \int [\hat{\Psi}, \hat{\Psi}^\dagger \hat{\Psi}^\dagger \hat{\Psi} \hat{\Psi}] d\mathbf{r} \\ &= \int [\hat{\Psi}, \hat{\Psi}^\dagger] \hat{h}_0 \hat{\Psi} + \hat{\Psi}^\dagger [\hat{\Psi}, \hat{h}_0 \hat{\Psi}] d\mathbf{r} \\ &\quad + \frac{g}{2} \int [\hat{\Psi}, \hat{\Psi}^\dagger] \hat{\Psi}^\dagger \hat{\Psi} \hat{\Psi} + \hat{\Psi}^\dagger [\hat{\Psi}, \hat{\Psi}^\dagger] \hat{\Psi} \hat{\Psi} + \hat{\Psi}^\dagger \hat{\Psi}^\dagger [\hat{\Psi}, \hat{\Psi} \hat{\Psi}] d\mathbf{r} \\ &= \hat{h}_0 \hat{\Psi}(\mathbf{r}, t) + g \hat{\Psi}^\dagger(\mathbf{r}, t) \hat{\Psi}(\mathbf{r}, t) \hat{\Psi}(\mathbf{r}, t). \end{aligned} \tag{A.10}$$

We can continue to simplify the equation of motion by considering a mean-field approach for a single macroscopically occupied state. In the case of Bose-Einstein condensation the lowest energy level is macroscopically occupied and so we decompose the field operator via

$$\hat{\Psi}(\mathbf{r}, t) = \hat{\psi}(\mathbf{r}, t) + \hat{\delta}(\mathbf{r}, t),$$

where $\psi(\mathbf{r}, t)$ is a field operator for the condensate and $\hat{\delta}(\mathbf{r}, t)$ is a field operator for the non-condensed atoms, whether that be atoms in higher states, atoms residing in the thermal cloud, or atoms influenced by quantum mechanical fluctuations.

We now make the Bogoliubov approximation [bogo47], a somewhat violent symmetry breaking approximation in which the condensate field operator is replaced by a classical field,

$$\hat{\psi}(\mathbf{r}, t) = \psi(\mathbf{r}, t) = \sqrt{N_0} \phi_0(\mathbf{r}, t),$$

where N_0 is the number of particles in the condensate. Written in this way, it is then possible to approximate the condensate density using $n(\mathbf{r}, t) = |\psi(\mathbf{r}, t)|^2$. Unfortunately a direct consequence of the action is that the physical state described by $\hat{\Psi}(\mathbf{r}, t)$ no longer satisfies the same symmetries as before. In particular, the total number of particles is not conserved. This approximation is justified by the understanding that as the condensate forms, it takes on a single phase, and all the particles in the condensate can be described by a single wavefunction. In addition, it is assumed that if there are many particles in the condensate, the exact value of N_0 does not effect the system state significantly, that is, $N_0 \approx N_0 + 1$. This approximation is essentially equivalent to the statement $\langle \hat{\Psi}(\mathbf{r}, t) \rangle = \psi(\mathbf{r}, t) \neq 0$, where $\langle \dots \rangle$ denotes the ensemble average. The non-condensed field operator $\hat{\delta}(\mathbf{r}, t)$ remains as an operator in the decomposition, and captures all the fluctuations around $\psi(\mathbf{r}, t)$. It is

generally assumed that $\langle \hat{\delta}(\mathbf{r}, t) \rangle = 0$.

In principle, the classical field $\psi(\mathbf{r}, t)$ is interpreted as the condensed atoms, however it can also be interpreted as the condensate atoms along with excitations of the system, as long as the occupation at high energy states $n_{i \gg 1}$ and the size of quantum fluctuations are both negligible. The classical field, or c-field, approaches can be used to model finite temperature effects by modelling part of the thermal cloud with highly populated modes below a certain momentum cutoff [c-field citations].

In the limit of $T \rightarrow 0$, all of the particles become part of the condensate, so that $N = N_0$. The contribution from the non-condensate atoms can be neglected, $\hat{\delta}(\mathbf{r}, t) = 0$, and the field operator is written $\hat{\Psi}(\mathbf{r}, t) = \psi(\mathbf{r}, t)$. In this case, the Heisenberg equation of motion in Equation A.10 reduces to

$$\begin{aligned} i\hbar \frac{\partial}{\partial t} \psi(\mathbf{r}, t) &= \hat{h}_0 \psi(\mathbf{r}, t) + g \psi^*(\mathbf{r}, t) \psi(\mathbf{r}, t) \psi(\mathbf{r}, t) \\ &= \left(-\frac{\hbar^2}{2m} \nabla^2 + V_{\text{ext}}(\mathbf{r}, t) + g |\psi(\mathbf{r}, t)|^2 \right) \psi(\mathbf{r}, t), \end{aligned}$$

the the so called Gross-Pitaevskii equation (GPE), also known as the nonlinear Schrödinger equation.

Finally, note that as the particle number is no longer strictly conserved, calculations should be performed within the grand canonical ensemble [Huang]. This approach leads to the modified Hamiltonian $\hat{H} \rightarrow \hat{H} - \mu \hat{N}$, where μ is the chemical potential and \hat{N} is the total number operator. The above derivations can be easily repeated with the modified Hamiltonian to obtain a physically equivalent version of the GPE with a chemical potential term,

$$i\hbar \frac{\partial}{\partial t} \psi(\mathbf{r}, t) = \left(-\frac{\hbar^2}{2m} \nabla^2 + V_{\text{ext}}(\mathbf{r}, t) + g |\psi(\mathbf{r}, t)|^2 - \mu \right) \psi(\mathbf{r}, t). \quad (\text{A.11})$$

A.3 Energy

A.4 Force

$$T_{jk} = \rho v_j v_k + p \delta_{jk} - \frac{\hbar^2}{4m^2} \rho \frac{\partial}{\partial x_j} \frac{\partial}{\partial x_k} \ln \rho \quad (\text{A.12})$$

$$F_k = \frac{\partial}{\partial t} \int_V J_k \, dV = - \int_V \frac{\partial}{\partial x_j} T_{jk} \, dV - \int_V \rho \frac{\partial}{\partial x_k} \left(\frac{V}{m} \right) \, dV \quad (\text{A.13})$$

Bibliography

- [1] A. J. Allen, E. Zaremba, C. F. Barenghi, and N. P. Proukakis, Phys. Rev. A **87**, 013630 (2013).
- [2] T. W. Neely, E. C. Samson, A. S. Bradley, M. J. Davis, and B. P. Anderson, Phys. Rev. Lett. **104**, 160401 (2010).
- [3] S. Taneda, J. Phys. Soc. Jpn. **11**, 302 (1956).
- [4] S. Taneda, J. Phys. Soc. Jpn. **50**, 1398 (1981).
- [5] M. Van Dyke, *An album of fluid motion* (Parabolic Press, Stanford, CA, 1982).
- [6] J. Maurer and P. Tabeling, EPL (Europhysics Letters) **43**, 29 (1998).
- [7] J. Salort, C. Baudet, B. Castaing, B. Chabaud, F. Daviaud, T. Didelot, P. Diribarne, B. Dubrulle, Y. Gagne, F. Gauthier, et al., Physics of Fluids **22**, 125102 (2010).
- [8] C. Nore, M. Abid, and M. E. Brachet, Phys. Rev. Lett. **78**, 3896 (1997).
- [9] M. Kobayashi and M. Tsubota, Phys. Rev. Lett. **94**, 065302 (2005).
- [10] A. W. Baggaley, J. Laurie, and C. F. Barenghi, Phys. Rev. Lett. **109**, 205304 (2012).
- [11] JETP Letters **80**, 479 (2004).
- [12] U. Frisch, *Turbulence. The legacy of A.N. Kolmogorov* (Cambridge University Press, Cambridge, 1995).
- [13] C. F. Barenghi, V. L'vov, and P.-E. Roche, *Velocity spectra of quantum turbulence: experiments, numerics and models* (2013), [arXiv:1306.6248](https://arxiv.org/abs/1306.6248).
- [14] M. R. Smith, D. K. Hilton, and S. Van Sciver, Phys. Fluids **11**, 1 (1999).
- [15] T. Zhang and S. Van Sciver, Nature Physics **1**, 36 (2005).
- [16] Y. Sergeev and C. Barenghi, J. Low Temp. Phys. **157**, 429 (2009).

- [17] R. Hänninen, M. Tsubota, and W. F. Vinen, Phys. Rev. B **75**, 064502 (2007).
- [18] S. Fujiyama and M. Tsubota, Phys. Rev. B **79**, 094513 (2009).
- [19] R. Goto, S. Fujiyama, H. Yano, Y. Nago, N. Hashimoto, K. Obara, O. Ishikawa, M. Tsubota, and T. Hata, Phys. Rev. Lett. **100**, 045301 (2008).
- [20] T. Frisch, Y. Pomeau, and S. Rica, Phys. Rev. Lett. **69**, 1644 (1992).
- [21] K. Sasaki, N. Suzuki, and H. Saito, Phys. Rev. Lett. **104**, 150404 (2010).
- [22] B. Jackson, J. F. McCann, and C. S. Adams, Phys. Rev. A **61**, 051603 (2000).
- [23] C. Nore, M. E. Brachet, and S. Fauve, Physica D **65**, 154 (1993).
- [24] T. Winiecki, J. F. McCann, and C. S. Adams, Phys. Rev. Lett. **82**, 5186 (1999).
- [25] T. Winiecki, B. Jackson, J. F. McCann, and C. S. Adams, Journal of Physics B: Atomic, Molecular and Optical Physics **33**, 4069 (2000).
- [26] C. Huepe and M. E. Brachet, Physica (Amsterdam) **140**, 126 (2000).
- [27] J. S. Stießberger and W. Zwerger, Phys. Rev. A **62**, 061601 (2000).
- [28] M. Crescimanno, C. G. Koay, R. Peterson, and R. Walworth, Phys. Rev. A **62**, 063612 (2000).
- [29] N. G. Berloff and P. H. Roberts, J. Phys. A **33**, 4025 (2000).
- [30] S. Rica, Physica D **148**, 221 (2001).
- [31] C. T. Pham, C. Nore, and M. E. Brachet, Comptes Rendus Physique **5**, 3 (2004).
- [32] B. Jackson, J. F. McCann, and C. S. Adams, Phys. Rev. Lett. **80**, 3903 (1998).
- [33] K. Fujimoto and M. Tsubota, Phys. Rev. A **83**, 053609 (2011).
- [34] T. Aioi, T. Kadokura, T. Kishimoto, and H. Saito, Phys. Rev. X **1**, 021003 (2011).
- [35] G. A. El, A. Gammal, and A. M. Kamchatnov, Phys. Rev. Lett. **97**, 180405 (2006).
- [36] I. Carusotto, S. X. Hu, L. A. Collins, and A. Smerzi, Phys. Rev. Lett. **97**, 260403 (2006).
- [37] C. Raman, M. Köhl, R. Onofrio, D. S. Durfee, C. E. Kuklewicz, Z. Hadzibabic, and W. Ketterle, Phys. Rev. Lett. **83**, 2502 (1999).
- [38] R. Onofrio, C. Raman, J. M. Vogels, J. R. Abo-Shaeer, A. P. Chikkatur, and W. Ketterle, Phys. Rev. Lett. **85**, 2228 (2000).

- [39] S. Inouye, S. Gupta, T. Rosenband, A. P. Chikkatur, A. Görlitz, T. L. Gustavson, A. E. Leanhardt, D. E. Pritchard, and W. Ketterle, Phys. Rev. Lett. **87**, 080402 (2001).
- [40] C. J. Pethick and H. Smith, *Bose-Einstein Condensation in Dilute Gases* (Cambridge University Press, Cambridge, 2002).
- [41] R. J. Donnelly, *Quantized Vortices in Helium II* (Cambridge University Press, Cambridge, 1991).
- [42] P. Nozières and D. Pines, *The Theory of Quantum Liquids II* (Addison-Wesley, Redwood City, 1990).
- [43] T. Winiecki, Ph.D. thesis, The University of Durham (2001).
- [44] A. C. White, C. F. Barenghi, and N. P. Proukakis, Phys. Rev. A **86**, 013635 (2012).
- [45] M. T. Reeves, T. P. Billam, B. P. Anderson, and A. S. Bradley, Phys. Rev. Lett. **110**, 104501 (2013).
- [46] A. W. Baggaley, C. F. Barenghi, A. Shukurov, and Y. A. Sergeev, EPL (Europhysics Letters) **98**, 26002 (2012).
- [47] T. Winiecki, J. F. McCann, and C. S. Adams, EPL (Europhysics Letters) **48**, 475 (1999).
- [48] D. H. Wacks, A. W. Baggaley, and C. F. Barenghi, Physics of Fluids **26**, 027102 (2014).
- [49] M. Blažková, D. Schmoranzer, L. Skrbek, and W. F. Vinen, Phys. Rev. B **79**, 054522 (2009).
- [50] D. I. Bradley, D. O. Clubb, S. N. Fisher, A. M. Guénault, R. P. Haley, C. J. Matthews, G. R. Pickett, V. Tsepelin, and K. Zaki, Phys. Rev. Lett. **95**, 035302 (2005).
- [51] A. Görlitz, J. M. Vogels, A. E. Leanhardt, C. Raman, T. L. Gustavson, J. R. Abo-Shaeer, A. P. Chikkatur, S. Gupta, S. Inouye, T. Rosenband, et al., Phys. Rev. Lett. **87**, 130402 (2001).
- [52] C. J. Foster, P. B. Blakie, and M. J. Davis, Phys. Rev. A **81**, 023623 (2010).
- [53] A. C. White, B. P. Anderson, and V. S. Bagnato, Proceedings of the National Academy of Sciences **111**, 4719 (2014).
- [54] C. F. Barenghi, L. Skrbek, and K. R. Sreenivasan, Proceedings of the National Academy of Sciences **111**, 4647 (2014).
- [55] C. F. Barenghi, R. Donnelly, W. Vinen, and eds., *Quantized Vortex Dynamics and Superfluid Turbulence* (Springer, Berlin, 2001).

- [56] N. G. Parker and C. S. Adams, Phys. Rev. Lett. **95**, 145301 (2005).
- [57] S. Middelkamp, P. J. Torres, P. G. Kevrekidis, D. J. Frantzeskakis, R. Carretero-González, P. Schmelcher, D. V. Freilich, and D. S. Hall, Phys. Rev. A **84**, 011605 (2011).
- [58] T. W. Neely, A. S. Bradley, E. C. Samson, S. J. Rooney, E. M. Wright, K. J. H. Law, R. Carretero-González, P. G. Kevrekidis, M. J. Davis, and B. P. Anderson, Phys. Rev. Lett. **111**, 235301 (2013).
- [59] W. J. Kwon, G. Moon, J.-y. Choi, S. W. Seo, and Y.-i. Shin, Phys. Rev. A **90**, 063627 (2014).
- [60] A. M. Mateo and V. Delgado, Phys. Rev. A **74**, 065602 (2006).
- [61] N. G. Parker and D. H. J. O'Dell, Phys. Rev. A **78**, 041601 (2008).
- [62] B. Jackson, N. P. Proukakis, C. F. Barenghi, and E. Zaremba, Phys. Rev. A **79**, 053615 (2009).
- [63] Y. Shin, private communication.
- [64] S. Choi, S. A. Morgan, and K. Burnett, Phys. Rev. A **57**, 4057 (1998).
- [65] M. Tsubota, K. Kasamatsu, and M. Ueda, Phys. Rev. A **65**, 023603 (2002).
- [66] E. Madarassy and C. F. Barenghi, Journal of Low Temperature Physics **152**, 122 (2008).
- [67] D. Yan, R. Carretero-González, D. J. Frantzeskakis, P. G. Kevrekidis, N. P. Proukakis, and D. Spirn, Phys. Rev. A **89**, 043613 (2014).
- [68] G. W. Stagg, N. G. Parker, and C. F. Barenghi, Journal of Physics B: Atomic, Molecular and Optical Physics **47**, 095304 (2014).
- [69] S. Nazarenko and M. Onorato, Journal of Low Temperature Physics **146**, 31 (2007).
- [70] C. Rorai, K. R. Sreenivasan, and M. E. Fisher, Phys. Rev. B **88**, 134522 (2013).
- [71] S. Prabhakar, R. P. Singh, S. Gautam, and D. Angom, Journal of Physics B: Atomic, Molecular and Optical Physics **46**, 125302 (2013).
- [72] M. Leadbeater, T. Winiecki, D. C. Samuels, C. F. Barenghi, and C. S. Adams, Phys. Rev. Lett. **86**, 1410 (2001).
- [73] S. Zuccher, M. Caliari, A. Baggaley, and C. Barenghi, Physics of Fluids **24**, 125108 (2012).
- [74] A. T. Powis, S. J. Sammut, and T. P. Simula, Phys. Rev. Lett. **113**, 165303 (2014).